# The Influence of Fe on Grain Boundary Mobility of Alumina

**Xinnian Wu**

# The Influence of Fe on Grain Boundary Mobility of Alumina

Research Thesis

In Partial Fulfillment of the
Requirements for the Degree of
Master of Science in Materials Engineering

**Xinnian Wu**

Submitted to the Senate of the Technion-Israel Institute of Technology

Nisan 5784 Haifa April 2024

The research thesis was done under the supervision of **Prof. W. D. Kaplan** and **Assoc. Prof. Yuanshen Qi** in the Department of Materials Science & Engineering at the Technion-Israel Institute of Technology and Guangdong Technion-Israel Institute of Technology, respectively.

# Acknowledgments

I thank my supervisors Prof. Wayne D. Kaplan and Assoc. Prof. Yuanshen Qi for the support, guidance, and help during the research.

Special thanks to Dr. Rachel Marder for the help in the first year. Thank you to my colleagues for their help, encouragement, and warm friendship.

Thank you to my family and friends. Thank me for the hard work and never giving up during these two years!

The generous financial help of the Guangdong Technion-Israel Institute of Technology is gratefully acknowledged.

# Ethical Statement

The author of this thesis states that the research, including the collection, processing and presentation of data, addressing and comparing to previous research, etc., was done entirely in an honest way, as expected from scientific research that is conducted according to the ethical standards of the academic world. Also, reporting the research and its results in this thesis was done in an honest and complete manner, according to the same standards.

# Table of Contents


Abstract ..... 1
List of Symbols ..... 2
List of Abbreviations ..... 5
List of Figures ..... 6
List of Tables ..... 8
1. Literature Survey ..... 9
1.1 Microstructure Evolution ..... 9
1.1.1 Grain Growth ..... 9
1.1.2 Grain Boundary Motion ..... 10
1.2 Microstructure Control ..... 15
1.2.1 Solid State Sintering ..... 15
1.2.2 The Influence of Dopants ..... 16
1.3 Model Material: α-alumina ..... 22
1.4 The Solubility Limit of Dopants in Alumina at 1600 °C ..... 23
1.5 The Influence of Dopants on Grain Boundary Mobility in Alumina ..... 25
1.5.1 Mg ..... 25
1.5.2 Ca ..... 26
1.5.3 Ti ..... 27
1.5.4 Si ..... 27
1.5.5 Fe ..... 27
2. Research Goals ..... 30
3. Experimental Methods ..... 31
3.1 Sample Processing ..... 31
3.1.1 Slip Casting ..... 31
3.1.2 Uniaxial Pressing ..... 31
3.1.3 Salt Infiltration ..... 32
3.1.4 Sintering ..... 33
3.1.5 Grain Growth ..... 34

# Table of Contents (Continued)


3.2 Characterization ..... 34
3.2.1 Relative Density ..... 34
3.2.2 Phase Determination by XRD ..... 35
3.2.3 Concentration Measurement by WDS ..... 35
3.2.4 Grain Size Measurement Based on SEM ..... 36
3.2.5 Grain Aspect Ratio Characterization by SEM-EBSD ..... 37
3.2.6 Valence State Measurement by XPS ..... 37
3.2.7 Grain Boundary Mobility Estimation ..... 38
3.2.8 Quantitative Fe Excess Measurement by STEM-EDS ..... 39
4. Results ..... 41
4.1 Relative Density and Dopant Concentration ..... 41
4.2 XRD Results ..... 42
4.3 Valence State of Fe Dopant ..... 42
4.4 Microstructure and Grain Growth ..... 45
4.5 Effective Grain Boundary Mobility ..... 50
4.6 Excess of Fe at Grain Boundaries ..... 53
5. Discussion ..... 55
5.1 The Influence of Fe Valence State on The Microstructure Evolution ..... 55
5.2 The Influence of Fe on Grain Growth ..... 59
5.3 The Influence of Fe on Grain Boundary Mobility ..... 60
6. Summary and Conclusions ..... 64
7. Future Work ..... 66
8. References ..... 67

# Abstract

The extent of grain growth is directly related to grain boundary (GB) velocity, which depends on GB energy and GB mobility. Therefore, GB mobility is one of the key parameters that dominate the microstructure evolution of polycrystalline materials. It has been widely reported that dopants and/or impurities can significantly affect GB mobility. Segregated solutes on α-$Al_2O_3$ (alumina) GBs can induce solute drag (such as Mg) or solute acceleration (such as Ca).

In this project, we used α-$Al_2O_3$ as a model material to study the influence of Fe on GB mobility. Undoped and Fe-doped polycrystalline $Al_2O_3$ samples were prepared and sintered at 1600°C for 2 h in air. Three batches of samples with equiaxed grains and Fe concentrations (**0.18 wt.%**, **0.71 wt.%**, and **1.26 wt.%**) below the solubility limit (8.9 wt.%) in $Al_2O_3$ at 1600 °C were characterized by conducting scanning electron microscopy and wavelength-dispersive X-Ray spectroscopy. After annealing at 1600°C in air for different durations, the grain size and the effective GB mobility were measured and determined, respectively. We found that doping alumina with Fe can retard grain growth, and the grain size and the effective GB mobilities decreased with the increasing Fe concentration. Moreover, the combined effects of Fe and Mg dopants on $Al_2O_3$ GB mobility were also studied. Both Mg and Fe reduced GB mobility, but Mg exhibited a stronger drag effect on alumina GB migration than that of Fe. We conducted scanning transmission electron microscopy combined with energy dispersive X-ray spectroscopy and determined the Fe excess at a specific GB in the alumina doped with 1.26 wt.% Fe to be 3.6±1.4 Fe atoms/$nm^2$, which was quantified with a measured detection limit of 1.8±0.6 Fe atoms/$nm^2$. We concluded that Fe at concentrations below the solubility limit reduced $Al_2O_3$ GB mobility by solute drag, similar to Mg.

In addition, we characterized the chemical state of Fe dopants in a **2.93 wt.%** Fe-doped $Al_2O_3$ that possessed elongated grains using X-ray photoelectron spectroscopy, and observed both $Fe^{2+}$ and $Fe^{3+}$ characteristic peaks. This could be the reason why the 2.93 wt.% Fe-doped $Al_2O_3$ presented anisotropic grain growth. Since $Fe^{3+}$ hinders GB motion and $Fe^{2+}$ was reported to enhance grain growth in $Al_2O_3$, we derived a hypothesis that the presence of divalent Fe resulted in an increase of the oxygen vacancy concentration near the GBs to compensate for the charge imbalance, and this may accelerate the GB motion. A selective adsorption of $Fe^{3+}$ and/or $Fe^{2+}$ on different GBs then resulted in an anisotropic grain growth.

# List of Symbols

| | |
|---|---|
| $A$ | total interface area |
| $A_{Al}$, $A_{Fe}$, | atomic masses of Al and Fe |
| $C\infty$ | bulk solute concentration |
| $C_{spec}$ | concentration of the element |
| $C_{std}$ | element concentration measured from the selected standard |
| $C_{lim,0.975}$ | limit of detection with a confidence probability of 97.5% |
| $d_0$ | average initial grain size |
| $D_{GB}$ | boundary self-diffusion coefficient |
| $D$ | dry weight |
| $E_b$ | binding energy of the atomic orbital from which the electron originates |
| $E_s$ | kinetic energies of the emitted electrons |
| $F_{GB}$ | driving force |
| f | site factor |
| $F_r$ | retarding force |
| $F_s$ | drag force |
| $F_0$ | intrinsic drag |
| F1, F2, F3, F4 | Fe-doped $Al_2O_3$ |
| FM1 | Fe and Mg co-doped $Al_2O_3$ |
| G | grain size |
| $\bar{G}$ | average grain size |
| $\overline{G_0}$ | initial average grain size |
| $\overline{G_t}$ | average grain size after annealing time t |
| $g_{ZAF}$ | ZAF correction factor for atomic number (Z), absorption (A), and characteristic fluorescence (F) |

# List of Symbols (Continued)

| | |
|---|---|
| $h\nu$ | energy of the photon |
| $I_{spec}$ | intensity of characteristic X-ray radiation from the specimen |
| $I_{std}$ | intensity measured from the selected standard |
| $I_{GB}$ | background intensity |
| $I_{Al}^{GB}$ | measured characteristic X-ray intensities of the Al in GB area |
| $I_{Fe}^{excess}$ | measured characteristic X-ray intensities of Fe elements excess in the GB area |
| $I_{Fe}^{GB}$ | measured characteristic X-ray intensities of the Al in the GB area |
| $I_{Fe}^{b}$ | intensity in the background under the elemental peak of Fe |
| $I_{Fe}^{grain\ 1}$, $I_{Fe}^{grain\ 2}$ | measured characteristic X-ray intensities of the Fe in grain 1 or grain 2 |
| K | rate constant |
| $K_0$ | grain growth factor |
| $k$ | the Boltzmann constant |
| k | rate constant |
| $k_{Fe/Al}$ | Fe–Al k-factor |
| $M_{GB}$ | GB mobility |
| $M_0$ | intrinsic mobility |
| M1 | Mg-doped $Al_2O_3$ |
| m | number of measurements |
| $M_{1min}$ | effective GB mobility of the sample annealed for 1 min |
| ppm | parts per million |
| $pO_2$ | oxygen partial pressure |
| $r_1$, $r_2$ | curvature radii of two grains, |

# List of Symbols (Continued)

| | |
|---|---|
| $t$ | migration time or annealing time |
| T | the absolute temperature |
| U0 | undoped $Al_2O_3$ |
| $v_{GB}$ | GB migration velocity |
| V | interaction volume |
| wt.% | weight percent |
| $\Delta P$ | pressure difference |
| $\gamma$ | surface and interface energy |
| $\gamma_{GB}$ | GB energy |
| $\Delta Q$ | activation energy for grain growth, |
| $\Omega$ | total ionic volume |
| $\delta$ | width of GB core |
| $\theta$ | dihedral angle |
| $\alpha$ | drag coefficient |
| $\beta^{-1}$ | velocity at which the boundary breaks away from the solute cloud |
| $\rho_{Al2O3}$ | theoretical density of $Al_2O_3$ |
| $\tau$ | single measurement time |
| $\phi$ | spectrometer work function |
| $\Gamma_{Fe}$ | amount of Fe excess at GBs |
| $\rho$ | density of the matrix |

# List of Abbreviations

| | |
|---|---|
| BC | band contrast |
| DFT | density function theory |
| EBSD | electron backscattered diffraction |
| EDS | energy dispersive X-ray spectrometry |
| EELS | electron energy loss spectroscopy |
| FIB | focused-ion beam |
| GB | grain boundary |
| IPF | inverse pole figure |
| RTP | ready-to-press |
| SEM | scanning electron microscope |
| STEM | scanning transmission electron microscope |
| *S* | suspended weight |
| S | area of the GB in the interaction volume |
| TLK | terrace ledge kink |
| TEM | transmission electron microscopy |
| WDS | wavelength-dispersive spectroscopy |
| *W* | saturated weight |
| XRD | X-ray diffraction |
| XPS | X-ray photoelectron spectroscopy |
| HAADF | high-angle annular dark-field |
| 2D, 3D | 2 dimensions, 3 dimensions |

# List of Figures

Figure 1: Atomic model for grain boundary migration (short-range motion of atoms) [9]. ..... 11

Figure 2: Illustration showing TLK model, terraces, ledges, kinks, and adatoms [14]. ..... 12

Figure 3: A high-angle annular dark-field (HAADF)-STEM micrograph of an edge-on tilt GB with the atomistic model of $SrTiO_3$ [18]. Nanometer length-scale steps are visible along the boundary (marked in yellow). In the atomistic solution green circles represent Sr, red circles represent O, and blue circles represent Ti. ..... 13

Figure 4: Schematic drawing showing the stop-and-go transformation kinetics induced by the dislocation lines parallel to the interfacial ledge; the lateral flow of the interfacial ledge is pinned at the dislocation core until the dislocation line climbs to the upper terrace [19]. ..... 14

Figure 5: Schematic illustration showing the basic phenomena during sintering and the two types of driving forces determining the sintering process [5]. ..... 16

Figure 6: The possible influence of composition on the mobility in a polycrystalline material (with many grain boundaries) [9]. ..... 17

Figure 7: Interaction of a GB with an immobile particle. (a) The approach of the boundary toward the particle. (b) Interaction between the grain boundary and the particle leads to a retarding force on the boundary. (c) Detailed geometry of the particle–GB interaction ( from reference [5]). .... 18

Figure 8: Schematics of the solute drag effect produced by the segregation of dopants to the grain boundaries. (a) Symmetrical distribution of the dopant in the region of a stationary GB. (b) For a moving boundary, the dopant distribution becomes asymmetric if the diffusion coefficient of the dopant atoms differs from that of the matrix atoms. The asymmetric distribution produces a drag on the boundary. (c) Breakaway of the GB from the dopant leaves a solute cloud behind [5]. ... 20

Figure 9: (a) Force-velocity behavior for intrinsic migration, (b) force-velocity relationship for solute drag only, and (c) total force-velocity behavior showing transition from solute drag limited migration at low F to near-intrinsic migration at high F [7]. ..... 21

Figure 10: Schematic drawing of the hexagonal (a) and rhombohedral (b) unit cells of a-$Al_2O_3$. The red spheres represent oxygen anions, and the black spheres represent aluminum cations [37]. ..... 22

Figure 11: Phase diagram of $Fe_2O_3$-$Al_2O_3$ system. The red dashed line marks 1600 °C and the related mole fraction, redrawn after Raghavan et al. [48]. ..... 24

Figure 12: A photograph of the infiltration system. ..... 33

Figure 13: Dark field STEM of a GB in a sample, demonstrating the regions scanned for EDS measurements of the GB excess. The selected areas for measurements are indicated in yellow boxes. ..... 40

Figure 14: XRD patterns from the undoped $Al_2O_3$ sample and doped $Al_2O_3$ samples with different dopant concentrations, sintered at 1600 °C for 2 h in air. Reflections from second phases were not detected. ..... 42

Figure 16: Secondary electron SEM micrographs (polished cross-section) of the microstructure of (a) undoped $Al_2O_3$, (b) 0.18 wt.% Fe-doped $Al_2O_3$, (c) 0.71 w.t% Fe-doped $Al_2O_3$, (d) 1.26 wt.% Fe-doped $Al_2O_3$, (e) 2.93 wt.% Fe-doped $Al_2O_3$ annealed for 2 h at 1600 °C in air. ..... 46

Figure 17: EBSD BC maps and IPF micrographs of undoped (a), 1.26 wt.% Fe-doped (b) and 2.93 wt.% Fe doped (c) samples annealed at 1600 ℃ for 2 h in air. The indexed rates are higher than 93%. ..... 48

Figure 18: Secondary electron SEM micrographs (on polished cross-sections) of the microstructure of Fe-doped $Al_2O_3$ (0.71 wt.%) annealed for (a) 1 min and (b) 4 h at 1600 °C in air. ..... 48

Figure 19: Grain size of undoped $Al_2O_3$ and $Al_2O_3$ doped with various concentrations of Fe (0.18 wt.%, 0.71 wt.%, 1.26 wt.%) after different annealing durations at 1600 ℃ in air. ..... 49

Figure 20: Grain size comparison of undoped, 1.26 wt.% Fe-doped, ~0.01 wt.% Mg-doped, and ~0.01 wt.% Mg and 0.41 wt.% Fe co-doped $Al_2O_3$ after different annealing durations at 1600 ℃ in air. ..... 50

Figure 21: Grain growth kinetics of undoped $Al_2O_3$ and $Al_2O_3$ doped with various concentrations of Fe. The slopes represent the values of the effective mobility of the different samples. The goodness of fit is shown as $R^2$-values. Grain growth kinetics of the sample annealed for 1 min was the setting as the initial site $M_{1min}$=0..... 51

Figure 22: Summary of grain growth kinetic of undoped, various Fe contents doped, Mg-doped and Mg-Fe co-doped $Al_2O_3$ annealed at 1600 ℃ in air for different durations. The goodness of fit is shown as $R^2$-values..... 52

Figure 23: (a) BF-STEM micrograph demonstrating the GB chosen for the EDS analysis. (b) HAADF-STEM micrograph showing three selected regions for EDS analysis using the spatial difference method. ..... 53

Figure 24: EDS spectra acquired from the interface region shown in Figure 23b. The spectrum from area#1 in grain No.1 adjacent to the GB is marked in gray; The spectrum acquired from area#2 including grain boundary is marked in red; and the spectrum from area#3 in grain No.2 adjacent to the GB is marked in blue. The Cu signal is from the TEM grid upon which the sample was mounted. ..... 54

Figure 25: Phase diagram of the $FeO$-$Fe_2O_3$ system. Dash-dot lines are oxygen isobars [2]..... 56

Figure 26: Green bodies and sintered dense specimens demonstrating the color change due to the evolution of the valance state of Fe dopant. ..... 57

Figure 27: Secondary electron SEM of anisotropic microstructure with superimposed dashed lines demonstrating the segregation of $Fe^{3+}$ and $Fe^{2+}$ on GBs. GBs controlled mainly by $Fe^{3+}$ and $Fe^{2+}$ segregation are highlighted in the red and green dashed lines, respectively. This is the 2.93 wt.% Fe-doped $Al_2O_3$ sample annealed at 1600 ℃ for 2 h in air. ..... 59

Figure 28: Effective GB mobility of undoped $Al_2O_3$ annealed in air, compared to effective mobility values from the literature. Redrawn from the data in [21]. ..... 61

# List of Tables

Table 1: The solubility limit of serval dopant species in alumina at 1600 ℃. ..... 23

Table 2: The average relative density and actual dopant concentration of samples. ..... 41

Table 3: Fe2p spectral fitting parameters: peak position (eV), peak area, FWHM value (eV), and Gaussian–Lorentzian ratio (%GL) (eV)..... 44

Table 4: The measured aspect ratio of 1.26 wt.% Fe-doped $Al_2O_3$ and 2.93 wt.% Fe-doped $Al_2O_3$ annealed at 1600 ℃ for 2h in air..... 48

Table 5: Effective grain boundary mobility of all tested samples..... 52

Table 6: The effective ionic radii of host ion and some dopants from literature and the size difference with trivalent Al. ..... 63

# 1. Literature Survey

## 1.1 Microstructure Evolution

### 1.1.1 Grain Growth

In crystalline materials, microstructure features including grain size, morphology, and distribution play a significant role in determining the physical and mechanical properties [1, 2]. The evolution of grains at elevated temperatures is determined by grain growth which is defined by an increase of the average grain size with time at the expense of disappearing small grains. This process is accompanied by atomic (or ionic) diffusion from the shrinking grains to the growing ones across grain boundaries (GBs), in a short range at the nanoscale. It is generally recognized that the driving force for grain growth is the local difference in GB curvature (pressure difference, $\Delta P$) between adjacent grains due to the surface tension of the boundary [3]. The pressure difference is presented as Eq. (1)[4],

$$\Delta P = \gamma_{GB}\left(\frac{1}{r_1}+\frac{1}{r_2}\right) = \frac{\alpha\gamma_{GB}}{G} = F_{GB} \qquad \text{Eq. (1)}$$

where ΔP is the pressure difference between the adjacent grains, $\gamma_{GB}$ is the specific GB energy (energy per unit area), $r_1$ and $r_2$ are the curvature radii of two grains, $\alpha$ is the geometric factor associated with the shape of grains, and G represents the grain size. $F_{GB}$ is the driving force for atoms or ions moving across GBs.

During the grain growth process, the phenomenon that a small number of grains grow rapidly to large sizes relative to the average size of the population is referred to as abnormal or discontinuous grain growth [1, 5]. While the histogram of the grain size distribution after normal grain growth shows only one peak (unimodal distribution), the grain size distribution after abnormal grain growth is bimodal and persists over time. It has been reported that the existence of a bimodal grain size distribution degrades the mechanical properties of ceramic material [5]. Although the reason for abnormal grain growth remains unclear, it is generally considered to

be associated with the formation of liquid phases and/or the presence of some specific impurities during the sintering and annealing processes [1].

Grain growth can be described by the change in grain size (d) as a function of time (t) [3, 6]:

$$d^n - d_0^n = K \cdot t \qquad \text{Eq. (2)}$$

where $d_0$ is the average initial grain size, n is an exponent depending on the growth mechanism (normal grain growth: n = 2), t is the time, and K is the rate constant:

$$K = K_0 \cdot exp(-\frac{\Delta Q}{kT}) \qquad \text{Eq. (3)}$$

where $K_0$ is the grain growth factor; ΔQ is the activation energy for grain growth, $k$ is the Boltzmann constant and $T$ is the temperature.

The thermodynamic driving force for grain growth is to decrease the total GB area and thus the total free energy of the system [3]. The kinetics of the grain growth are determined by the GB mobility and GB energy, which depend on temperature, pressure, and dopant concentration (including gas partial pressures).

### 1.1.2 Grain Boundary Motion

The movement of a GB is via the "short" diffusion process whereby atoms or ions move from the shrinking grain across the GB to the growing grain. Under the local driving force of curvature, the atoms move from the convex to concave interface, leading to GB migration towards the opposite direction as presented in Figure 1. Recently Rohrer et al. reviewed the mechanisms of GB migration and summarized three prevailing models: the rate theory model, the terrace-ledge-kink model, and the disconnection model [7].

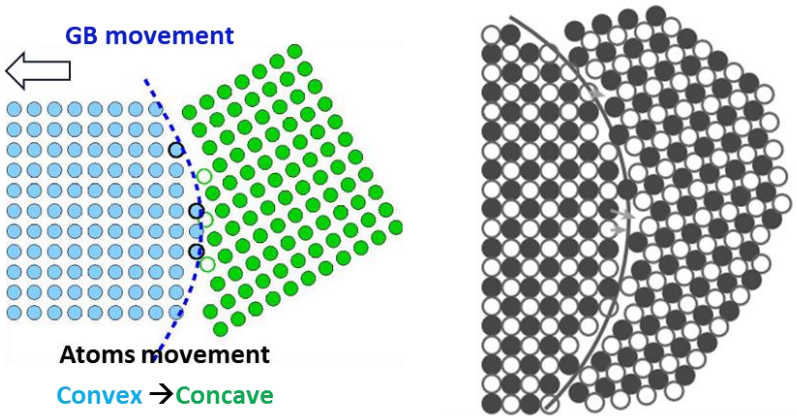


Figure 1: Atomic model for grain boundary migration (short-range motion of atoms) [8].

## Rate Theory Model

In the classical rate theory model, GB migration velocity determines the rate of grain growth, and it depends on GB mobility and GB driving force. At a steady state, the driving force is balanced by the total drag force which includes several components: intrinsic drag, solute drag, and the drag from pores or precipitates [6]. The velocity of GB migration, $v_{GB}$, is proportional to the curvature-induced driving force ($F_{GB}$), which is the product of the mean curvature $k$, and GB energy $\gamma_{GB}$ [6, 7] as shown in Eq. (4) [4].

$$v_{GB} = M_{GB} \cdot F_{GB} = M_{GB} \cdot k \cdot \gamma_{GB} \qquad \text{Eq. (4)}$$

where the proportionality constant is the GB mobility ($M_{GB}$) [9], and it can be obtained from the normalization of $v_{GB}$ and $F_{GB}$.

When the migration velocity is limited only by the diffusion of atoms across GBs, i.e., no other drag forces are acting on the boundary other than the intrinsic drag, the GB mobility is the intrinsic mobility $M_0$ and can be approximated at steady state as [6]:

$$M_0 = \frac{v_{GB}}{F_{GB}} = \frac{f D_{GB} \Omega}{\delta k T} \qquad \text{Eq. (5)}$$

where $D_{GB}$ is the boundary self-diffusion coefficient of the slower atoms for diffusion across the GB; Ω is the total ionic volume divided by the number of slow diffusing atoms, $\delta$ is the width of the GB core. The site factor, $f$, reflects the density of boundary core sites associated with high jump probabilities.

GB mobility is therefore the key kinetic parameter that dominates the velocity of GB motion. It is critical to determine the GB mobility in order to predict and control the grain growth.

Terrace-Ledge-Kink Model

Based on the observation that GB exhibits a step-like structure, Gleiter et al. first proposed that GB structure can be described by a terrace ledge kink (TLK) model, see Figure 2. Based on this theory, steps on a GB move via the absorption and emission of atoms [10, 11], and the GB migration occurs through the diffusion of atoms on the terrace plane, then along a ledge site, and finally to a kink site. This model is widely accepted [7, 12].

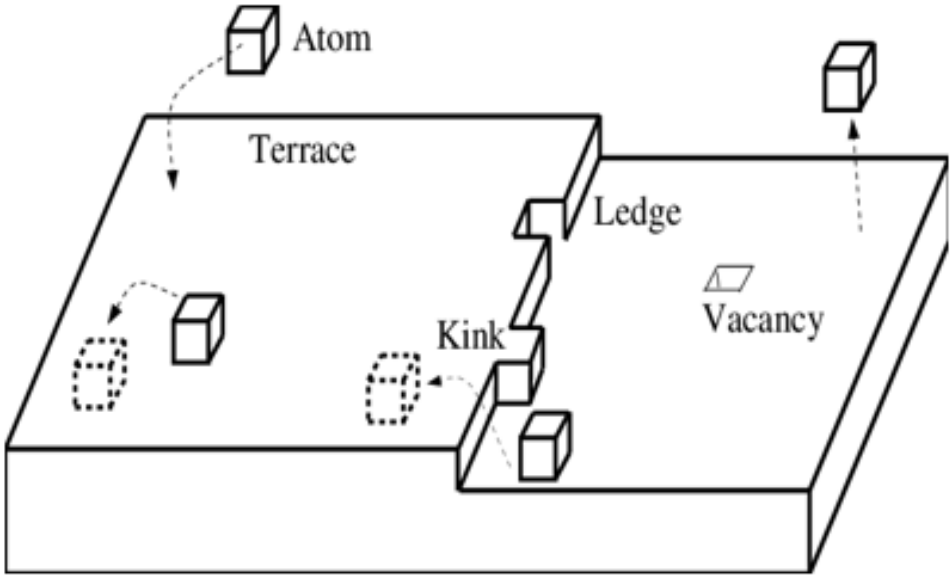


Figure 2: Illustration showing TLK model, terraces, ledges, kinks, and adatoms [13].

Disconnection Model

Disconnections are defined as line defects characterized by combined step and/or dislocation features at GBs [7, 14-16]. It is widely acknowledged that disconnections play an important and active role in the atomistic mechanism of GB migration. Disconnections can glide conservatively due to their Burgers vectors within the GB plane. As a result of their step feature, their motion on the GB plane can lead to the GB moving in the direction normal to the GB plane [16]. Sternlicht et al. identified the dislocation component of disconnections on tilt GBs in $SrTiO_3$ by conducting aberration-corrected transmission electron microscopy (TEM) characterization (see Figure 3) [17]. Sun et al. and Wang et al. directly observed the movement of disconnections in metal at the atomic scale through in-situ heating characterization in TEM [18, 19], and Sun et al. also simulated the stop-and-go transformation of disconnections using density functional theory (DFT) modeling, as illustrated in Figure 4.

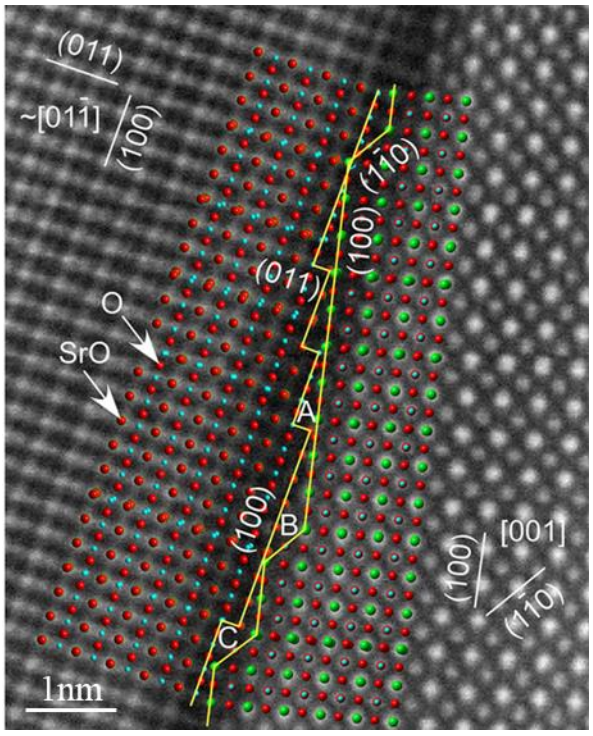


Figure 3: A high-angle annular dark-field (HAADF)-STEM micrograph of an edge-on tilt GB with the atomistic model of $SrTiO_3$ [17]. Nanometer length-scale steps are visible along the boundary (marked in yellow). In the atomistic solution green circles represent Sr, red circles represent O, and blue circles represent Ti.

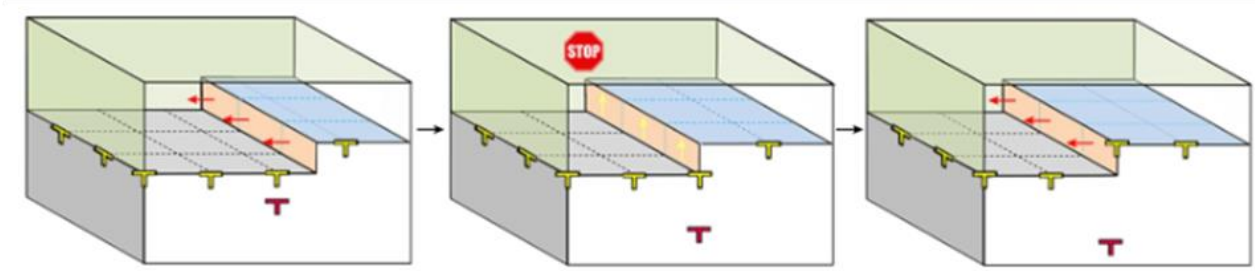


Figure 4: Schematic drawing showing the stop-and-go transformation kinetics induced by the dislocation lines parallel to the interfacial ledge; the lateral flow of the interfacial ledge is pinned at the dislocation core until the dislocation line climbs to the upper terrace [18].

## 1.2 Microstructure Control

Typically, regulating GB migration and consequently grain size is the primary approach to controlling microstructure, which is the major factor determining many of the mechanical, electrical, optical, and magnetic properties of ceramics [1]. Sintering is an essential process for densification and producing desired microstructures in almost all ceramic materials. Therefore, controlling sintering parameters including the heating scheme and atmosphere is a critical step in tailoring the final microstructure. Another effective method is to modify the chemical composition of the starting powder through doping. Chemical segregation of solutes at GBs can affect their velocity. Several studies have reported on the impact of dopants and/or impurities on GB migration[1, 4, 6, 20-23]. In this section, we first discuss the processing control – sintering, and then the chemical composition control – doping.

### 1.2.1 Solid State Sintering

Sintering is a process in which the green body, i.e., the compressed powder transforms into a condensed compact by heating and possible application of pressure [1]. Sintering can occur in the presence or absence of a liquid phase. In the absence of a liquid phase, the process is referred to as solid-state sintering[1, 2]. During sintering, changes in grain size, grain shape, pore size, pore shape, and volume fraction of pores occur simultaneously. The primary driving force behind sintering at the macroscopic level is the reduction of excess surface or interface energy of the system. The driving force can be expressed in Eq. (6) [24].

$$\Delta(\gamma A) = \Delta\gamma A + \gamma\Delta A \qquad \text{Eq. (6)}$$

where $(\gamma A)$ is the total interfacial [1]energy, $\gamma$ is the interface energy, and $A$ is the total interface area. This reduction can occur through two typically competing mechanisms (resulting in two processes): (1) the reduction of the total surface area

[1] Here "interface" and "surface" are identical, where the surface is an interface between a solid (or liquid) and the gas phase.

by the increase of the particle size, which leads to grain coarsening, and/or (2) the elimination of solid/vapor interfaces with high surface energy and the creation of GBs with relatively lower energy, which finally leads to densification (Figure 5). These two processes, i.e., grain coarsening and densification occur simultaneously during sintering. The balance between these two processes is critical to achieving the desired material properties and is an important area of study in the field of ceramics. For instance, to facilitate the densification and thus to obtain near theoretical dense ceramics, grain growth (grain coarsening) should be inhibited until the densification has been completed.

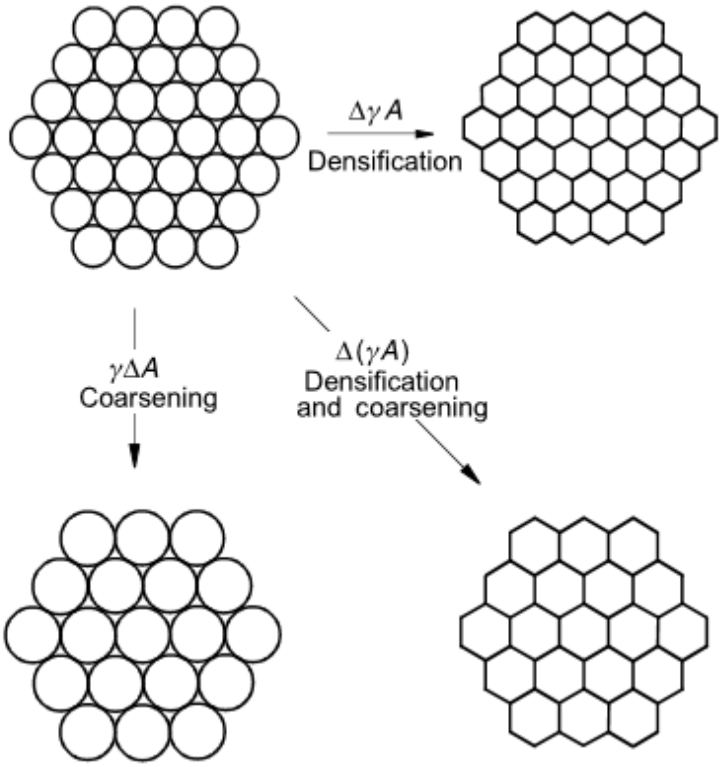


Figure 5: Schematic illustration showing the basic phenomena during sintering and the two types of driving forces determining the sintering process [4].

### 1.2.2 The Influence of Dopants

Since 100% pure ceramics do not exist, the powder utilized for sintering ceramic materials will always contain certain levels of impurities, and within limits of the

solubility limit it is a solid solution system containing a small amount of dopants (solutes) in a solid solvent. The presence of these impurities can significantly affect the microstructure. Dopants and impurities tend to segregate preferentially at different types of GBs, thereby altering relative GB mobility and energy. The influence can be categorized into two parts based on the solubility limit at the processing temperature, as described schematically in Figure 6. Doping at concentrations above the solubility limit can result in the precipitation of secondary phases, which may manifest as solid or liquid particles [25]. The solid particles subsequently reduce GB mobility by introducing Zener drag. Conversely, liquid particles have a tendency to greatly enhance GB mobility by forming liquid films along grain boundaries [4]. If the dopant concentration is below the solubility limit, the solutes can segregate at GBs (and other defects) if by doing so the excess surface energy is reduced, and can introduce solute drag [1, 4, 6] or solute acceleration of GB motion [22].

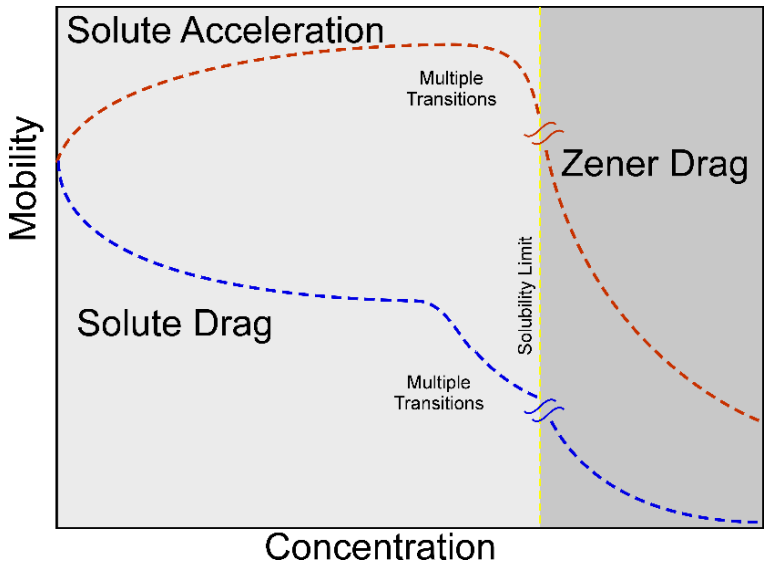


Figure 6: The possible influence of composition on the mobility in a polycrystalline material (with many grain boundaries) [8].

## Zener Drag

When the dopant concentration is above the solubility limit at the sintering temperature, solid second phase(s) could precipitate from the matrix and contribute to a pinning force at GBs. Zener and Smith first developed a quantitative model to

explain particle-inhibited GB migration [26, 27]. In this model, spherical, insoluble, and immobile particles were considered to be randomly distributed in the polycrystalline solid [4]. As presented in Figure 7, when a GB intersects a particle, its further movement is hindered by the particle. When precipitates are formed at GBs, the equivalent movement of GBs requires additional work compared with GBs without precipitates. This additional work manifested itself as a retarding force on the boundary [4]. Based on the driving force for GB movement as exhibited in Eq. (1), the retarding force of the inclusion acting on the boundary is the GB tension, which can be decomposed as a drag in the direction opposite to the direction of GB movement (Figure 7c). Then the retarding force exerted by the inclusion on the whole boundary can be expressed as:

$$F_r = (\gamma_{GB} \cos\theta)(2\pi r \sin\theta) \qquad \text{Eq. (7)}$$

where $F_r$ is the retarding force i.e. the Zener drag, $r$ is the radius of the inclusion, and $\theta$ is the dihedral angle between the mean surface of the GB and the interface of the inclusion.

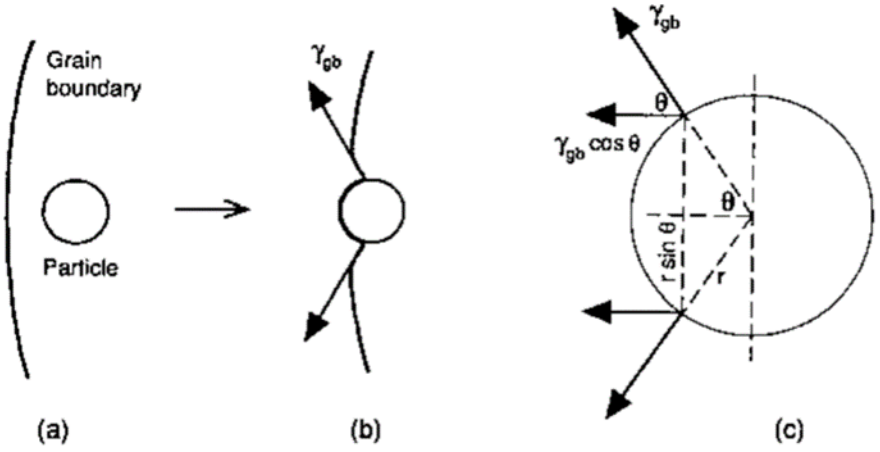


Figure 7: Interaction of a GB with an immobile particle. (a) The approach of the boundary toward the particle. (b) Interaction between the grain boundary and the particle leads to a retarding force on the boundary. (c) Detailed geometry of the particle–GB interaction ( from reference [4]).

Solute Drag

When the dopant concentration is below the solubility limit at the sintering temperature, the existence of certain dopants and impurities could cause solute drag and slow down the GB motion. A related atomistic theory was first developed by Lücke and Detret [28]. They predicted the GB velocity is determined by an impurity drag effect at conditions of high concentration or low driving force, while under low concentration or high driving force conditions, the breakaway occurred so the GB was not held back by the foreign atoms. Then the theory was quantitatively and concisely developed by Cahn [29], and Lücke and Stüwe [30]. They detailed the drag effect and found it depends on the difference between the GB velocity and the solute diffusivity, and the solute-GB interactions [29]. According to their model, the solute can be either attracted to or repelled from the GBs due to the interaction potential. This drives the solute to diffuse in the direction of GB migration. Solutes could segregate to a GB and create a concentration profile (sometimes called a solute cloud) in the vicinity of the GB if their excess lowers the GB energy. For a hypothetical stationary boundary, this concentration profile is symmetrical (ignoring atomistic structural differences on the two sides of the GB), and the interaction forces on both sides balance each other out (see Figure 8a). When the GB starts to migrate, an asymmetric solute profile with respect to the GB plane occurs because the diffusivities are different between the solute and matrix atoms (see Figure 8b). If the driving force for the GB migration is high enough, the boundary can eventually break away and detach from the high solute concentration profile as illustrated in Figure 8c.

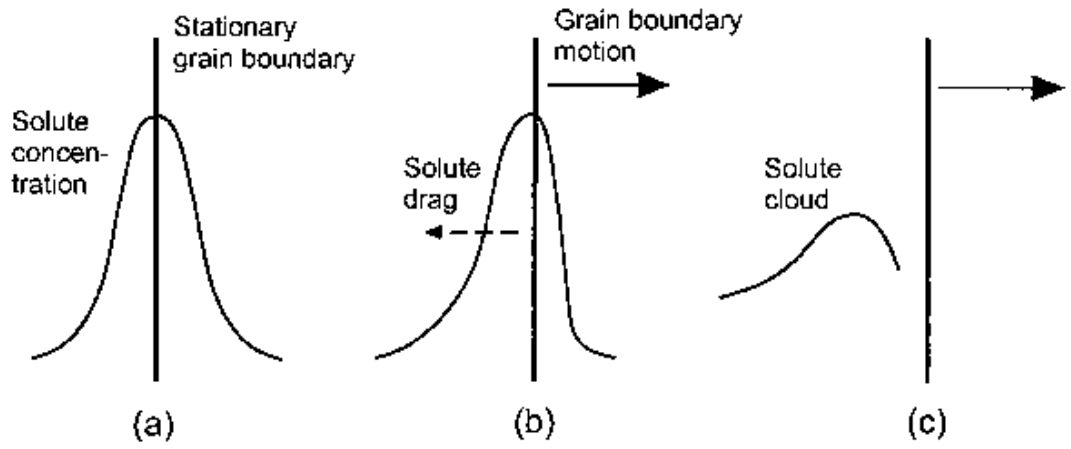


Figure 8: Schematics of the solute drag effect produced by the segregation of dopants to the grain boundaries. (a) Symmetrical distribution of the dopant in the region of a stationary GB. (b) For a moving boundary, the dopant distribution becomes asymmetric if the diffusion coefficient of the dopant atoms differs from that of the matrix atoms. The asymmetric distribution produces a drag on the boundary. (c) Breakaway of the GB from the dopant leaves a solute cloud behind [4].

The asymmetric solute concentration profile can impose a drag force $F_s$, namely solute drag, on the GB at steady state. The drag force could reduce the driving force for GB movement. The magnitude of the solute drag for both low and high boundary velocities can be estimated [29]:

$$F_s = \frac{\alpha C_\infty v_{GB}}{[1 + (\beta v_{GB})^2]} \qquad \text{Eq. (8)}$$

where $\alpha$ is the drag coefficient which means the solute drag force per unit velocity and per unit solute concentration in the low boundary velocity limit, $C_\infty$ is the bulk solute concentration, $v_{GB}$ is the GB velocity, and $\beta^{-1}$ defines the velocity at which the boundary breaks away from the solute cloud. α depends on temperature, the solute diffusivity in the region near GB, and the absolute magnitude of the solute-GB interaction energy [4, 6].

The total drag force on the boundary is the sum of the intrinsic drag $F_0$ and the solute drag force due to the dopant atoms $F_s$, as expressed in Eq. (9).

$$F = F_0 + F_s = \frac{v_{GB}}{M_0} + \frac{\alpha C_\infty v_{GB}}{[1 + (\beta v_{GB})^2]} \qquad \text{Eq. (9)}$$

where $M_0$ is the intrinsic mobility as mentioned above. The force-velocity behavior for intrinsic migration and/or solute drag limited migration is described in Figure 9.

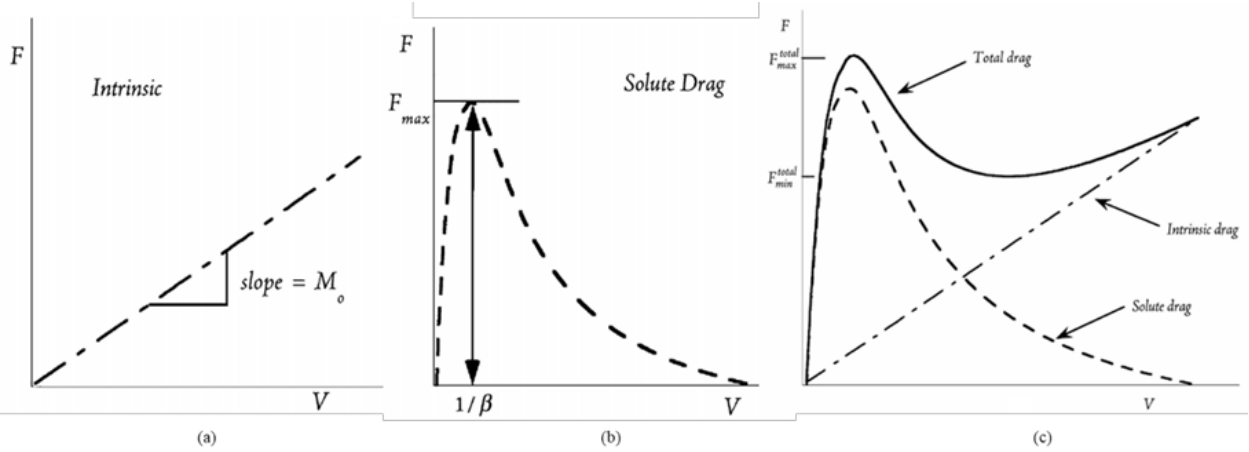


Figure 9: (a) Force-velocity behavior for intrinsic migration, (b) force-velocity relationship for solute drag only, and (c) total force-velocity behavior showing transition from solute drag limited migration at low F to near-intrinsic migration at high F [6].

## Solute Acceleration

Apart from the above-described solute drag effect that hinders the GB migration, in some cases, solute segregation to the GB could also introduce solute acceleration on GB movement by increasing the GB mobility. There have been a few studies that demonstrated this solute acceleration effect in alumina [20-22, 31] and yttrium aluminum garnet (YAG) [32, 33]. Moshe et al. and Akiva et al. discovered that 13 ppm CaO dopants (below the solubility limit) enhanced grain growth and increased GB mobility in alumina from $2.7 \times 10^{-15}\ m^2/s$ to $3.5 \times 10^{-15}\ m^2/s$ due to an increase in oxygen vacancy concentration in the vicinity of the GBs regions [20, 22]. Zamir et al. also observed that $ZrO_2$, MgO, and $SiO_2$ dopants can increase the GB mobility of YAG (without any secondary phases, intergranular films, or bulk liquids at GBs) as a result of the generation of dopant cations vacancies and/or O vacancies to enhance GB motion [33].

## 1.3 Model Material: α-alumina

α-alumina (α-$Al_2O_3$) is known as sapphire in its single crystal form and alumina or corundum in the polycrystalline form. α-alumina is the only structure identified to be thermodynamically stable in many metastable polymorphs of aluminum oxide [34]. The theoretical density of monolithic alumina calculated by Swanson et al. is 3.987 g/cm$^3$, and the melting point is 2072 ℃ [4, 35]. Two alternative ways based on a rhombohedral or a hexagonal unit cell are used to describe its structure. The schematic drawing of these two alternatives, i.e., hexagonal (with 30 atoms per unit cell) and rhombohedral (with 10 atoms per unit cell) are presented in Figure 10 [36].

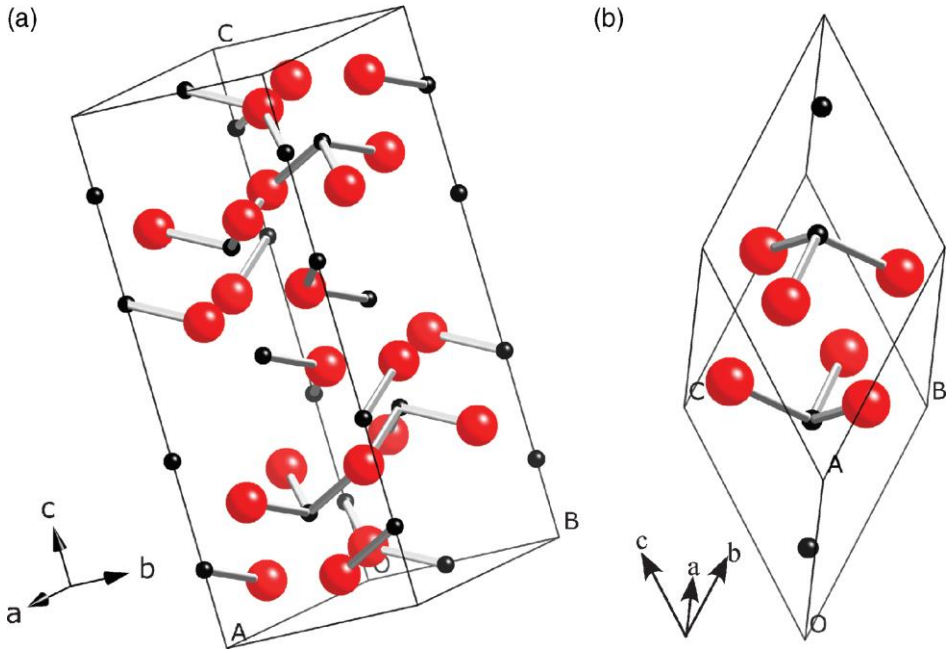


Figure 10: Schematic drawing of the hexagonal (a) and rhombohedral (b) unit cells of a-$Al_2O_3$. The red spheres represent oxygen anions, and the black spheres represent aluminum cations [36].

Alumina has many excellent mechanical and functional properties, such as good wear resistance and high thermochemical stability [20]. It has been applied as biomedical implants (such as dental implantations and hip replacements), wear-resistant coatings on armored vehicles, thermal barriers (refractories), and ceramic matrix nanocomposite [37-39]. α-alumina has been extensively investigated for decades as a paradigm for oxide ceramics, especially about the influence of dopants

and impurities on the sintering process, grain growth, GB migration, and microstructure-dependent engineering properties [22, 40].

## 1.4 The Solubility Limit of Dopants in Alumina at 1600 ℃

At a given temperature and pressure, the solubility limit is defined as the maximum concentration of solute that can be dissolved within the matrix without forming a second phase. From section 1.2.2 we know that it is important to determine the solubility limit of a dopant in a matrix at the processing temperature to fully engineer a microstructure. The solubility limit of several dopants of interest in α-alumina at 1600 ℃ are shown in Table 1.

Table 1: The solubility limit of serval dopant species in alumina at 1600 ℃.

| Dopants | Solubility limit [at. ppm] | References |
|---|---|---|
| $Ca^{2+}$ | 51±1 | [41, 42] |
| $Mg^{2+}$ | 132±11 | [43] |
| $Si^{4+}$ | 188±7 | [44] |
| Fe | 81,000 (in air) | to be published |
| $Cr^{3+}$ | completely miscible | [45, 46] |

The solubility limit of iron (Fe) in α alumina at 1600 ℃ was also determined by our group and is going to be published. The measured solubility limit is 81,000 ppm, which is 8.9 wt.%. This value meets the agreement with the binary phase diagram in Figure 11, and it is notable that the solubility limit is relatively high and close to 9 mole fractions marked by the red dashed line. In addition, according to the phase diagram of $Cr_2O_3$ and alumina ($Al_2O_3$), Cr ions are fully soluble and completely miscible in $Al_2O_3$.

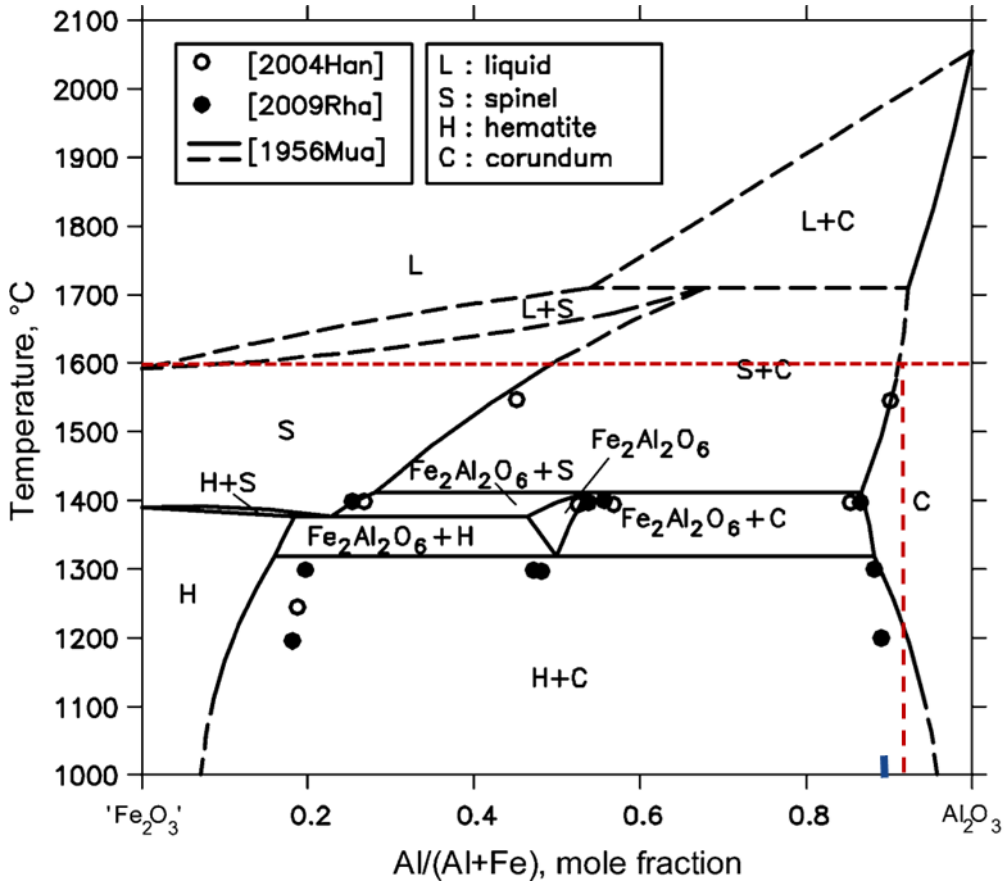


Figure 11: Phase diagram of $Fe_2O_3$-$Al_2O_3$ system. The red dashed line marks 1600 °C and the related mole fraction, redrawn after Raghavan et al. [47].

## 1.5 The Influence of Dopants on Grain Boundary Mobility in Alumina

Studies on the influence of dopants mostly focus on the relationship between sintering parameters leading to the microstructure and thus properties of $Al_2O_3$ [21, 22, 40, 48, 49]. The influence of dopants on GB mobility has been recognized as the determining factor of controlling grain size. Powers and Glaeser discussed the methods of experimental measurement of GB mobility and the dopant effects of Mg and Ti dopants on the GB mobility of ceramics material including $Al_2O_3$ [6]. In ceramics, directly measuring the GB mobility is challenging because it is difficult to produce fully dense and pure ceramics. Solutes, inclusions, pores, and secondary phases could exert drag force on the GB and affect the GB mobility. Nonetheless, several studies have managed to measure the GB mobility in undoped and doped $Al_2O_3$ to investigate the influence of solutes without directly addressing the influence of trace elements in the starting powder. The effects of Mg, Ca, Ti, Si, and Fe on alumina are summarized below.

### 1.5.1 Mg

The most studied solute in $Al_2O_3$ is MgO. Grimes used atomistic simulations to predict the preferred solution mechanism of MgO in $Al_2O_3$ to be self-compensating, which leads to the formation of interstitial Mg ions [50]. Berry and Harmer estimated the density and the grain size of $Al_2O_3$ with and without 250 ppm MgO and found MgO solutes can increase the densification rate during sintering [51]. They concluded that MgO mainly lowered the GB mobility rather than affecting the grain size/density curve. Johnson and Coble studied MgO-doped $Al_2O_3$ with secondary phases and determined that the well-known secondary phase theory was not the reason for the enhanced densification of sintered $Al_2O_3$ with MgO dopant [52]. Bennison et al. studied the effect of MgO as a solute on sintering and the kinetics of grain growth in $Al_2O_3$ as well [48, 53]. They prepared fully dense 200 ppm MgO doped and undoped $Al_2O_3$ samples and discovered that MgO retarded GB migration and reduced GB mobility by impurity drag and developed more uniform

microstructures. It was reported the primary role of MgO is to suppress GB motion and hence hinder grain growth [48, 53].

It is worth noting the measurement of the solubility limit of MgO in $Al_2O_3$ by Miller et al. using wavelength-dispersive spectroscopy (WDS) mounted on a scanning electron microscope (SEM) and the result was 132±11 ppm at 1600 ℃ [43]. Akiva experimentally measured the GB mobility of undoped and 23 ppm MgO doped $Al_2O_3$ at 1600 ℃ and demonstrated that doped MgO with a concentration below the solubility limit could decrease the GB mobility from $2.7\times 10^{-15}$ $m^2/s$ to $1.5\times 10^{-15}$ $m^2/s$ [20].

### 1.5.2 Ca

Regarding CaO in $Al_2O_3$, it has been shown that it causes a different effect than that of MgO with respect to grain geometry and GB mobility [20]. Altay et al. measured the Ca excess at GBs in different Ca doping levels (0~1000 ppm) and revealed that Ca caused elongated grain morphology when it excess exceeded 3–4 Ca atoms/$nm^2$ and abnormal grain growth when it excess exceeded 4.5 Ca atoms/$nm^2$ [54]. Bae and Baik also observed abnormal grain growth in 30 ppm CaO-doped $Al_2O_3$ [55].

Akiva et al. determined the solubility limit of CaO in $Al_2O_3$ to be 51±1 ppm at 1600 ℃ by performing WDS. They first measured the effective GB mobility of $Al_2O_3$ with 13 ppm CaO, which was experimentally confirmed to be below the solubility limit, and then detected the Ca excess at the GB. It was found that adding CaO as a solute in $Al_2O_3$ can lead to an increase in GB mobility and a platelike morphology which is associated with the increased mobility of non-basal lattice planes, such as $(10\bar{1}0)$ [20, 41]. Moshe et al. also experimentally studied the influence of CaO on $Al_2O_3$ GB mobility in a range of concentrations below the solubility limit. This demonstrated that CaO increases the rate of grain growth and mobility with increasing dopant levels, differing from MgO which reduces GB by solute drag. The increased mobility was reported due to Ca segregation that caused an increase in O vacancy concentration in the vicinity of the GBs, thus facilitating faster GB motion [22].

### 1.5.3 Ti

Doping $Al_2O_3$ with $TiO_2$ was also observed to increase the rate of sintering and enhance anisotropic abnormal grain growth with an increase in dopant concentration. This is presumably due to preferential Ti segregation to certain types of GBs and led to a change of GB energy and mobility or the formation of a liquid phase that selectively wets certain GBs [56, 57]. Powers et al. quantified that Ti significantly enhances GB mobility by using the seed growth method. Their sintering studies in a vacuum showed that the dopant valence influences microstructure development. $Ti^{4+}$ showed an ability to promote faceted grain growth while $Ti^{3+}$ is beneficial to an equiaxed microstructure in $Al_2O_3$ [6, 58, 59]. Despite the enhancement of Ti dopant at the GB mobility derived from this study, an accurate measurement of the solubility limit of Ti element in polycrystalline $Al_2O_3$ with high purity has not been published, to the best of our knowledge. Reported solubility limits vary widely as summarized by Kitayama et al. [60].

### 1.5.4 Si

The influence of $SiO_2$ as an impurity often presented in the system of alumna has been studied by several groups. It was reported that with an increase in $SiO_2$ concentration grains transferred from normal growth to abnormal growth [61]. In Dillon and Harmer's work, their results showed that 200 ppm $SiO_2$ in $Al_2O_3$ resulted in a higher GB mobility, but the mobility was not increased with dopant content (500 ppm $SiO_2$ doped $Al_2O_3$ had a lower GB than that of 200 ppm). They considered the 200 ppm solubility limit of $SiO_2$ according to the reference [61] in $Al_2O_3$ without technical quantification [62]. Moshe et al. determined the solubility limit of Si in $Al_2O_3$ at 1600 ℃ by using WDS on water-quenched $Al_2O_3$ samples saturated with Si and reported it to be 188±7 ppm [44].

### 1.5.5 Fe

The investigation of the influence of Fe on $Al_2O_3$ has been started since the 1970s. The studies were mainly focused on sintering, valence states, and mechanical properties of Fe-doped $Al_2O_3$. Rao and Cutler studied the effect of Fe oxide dopant

on the sintering kinetics of $Al_2O_3$ by using $Fe^{3+}$ as initial dopants and sintered samples in different atmospheres (in air, and in $N_2$ with 132 ppm $O_2$). They found the changes in Fe valence states from $Fe^{3+}$ and $Fe^{2+}$, and revealed that $Fe^{2+}$ ions enhanced the sintering rate of $Al_2O_3$ [63]. Specifically, FeO was found to promote grain growth more than densification and was beneficial to the sintering of MgO-doped $Al_2O_3$. These $Al_2O_3$ samples were doped with 250 ppm high-purity $Fe(NO)_3$ and sintered at 1620℃ in a graphite furnace with flowing nitrogen gas [64]. After studying $Al_2O_3$ doped with various $Fe(NO_3)_3{\cdot}9H_2O$ concentrations, Tartaj et al. discovered that the addition of $\alpha$-$Fe_2O_3$ resulted in anisotropic grain growth of lath-like grains at a temperature higher than 1300℃ in air. This may be due to the presence of $Fe^{2+}$ which significantly improved the mass transport during sintering [65]. Drahus et al. focused on studying the effect of the Fe valence state on $Al_2O_3$ densification and grain growth as well by carrying out experiments under both oxidizing (flowing air) and reducing conditions ($N_2/H_2$ mixture, oxygen partial pressure ($pO_2$) ~ $5.1 \times 10^{-14}$) at 1350℃. They reported the addition of 1000 ppm Fe reduced the densification rate and also retarded the grain growth in air but the 1000 ppm Fe dopants increased the densification rate under reducing atmosphere conditions [66].

Lessing et al. studied the influence of Fe on the creep of polycrystalline $Al_2O_3$ using $Fe^{3+}$ as an initial dopant and found that a high $Fe^{2+}$ content in the solid solution could lead to viscous Coble creep by dramatically enhancing Al lattice diffusion and oxygen GB diffusion (rate limited the creep) [67]. Fe-doped $Al_2O_3$ was studied from the perspective of texture development as a substrate for carbon nanotube growth since it exhibited potential as an available and low-cost catalyst for carbon nanotube synthesis [68]. Heiba et al. discovered that Fe ions could effectively tailor the band structure and narrow the band gap energy of $Al_2O_3$, and change photoluminescence emission peaks in $Al_2O_3$ [69]. In the compressive creep test, the $Fe^{2+}$ cations were found to show an acceleration in the deformation rates while the oxidation of $Fe^{2+}$ resulted in the dissolution of the $FeAl_2O_4$ spinel precipitates finally slowing down the deformation rate [70]. Rhee et al. studied the sintering of 1 wt.% Fe-doped $Al_2O_3$ at 1600℃ in both reducing and oxidizing conditions. They reported the presence of

Fe precipitates at triple junctions in the reducing atmosphere (pointed out that the solubility of $Fe_2O_3$ in $Al_2O_3$ is about 3 wt.% at $pO_2$ of ~0.03 atm.). Meanwhile, in the oxidizing atmosphere, precipitates could dissolve into grains near the sample surface and cause improved mechanical properties [71].

The change of the Fe valence state is inevitable in the sintering process. It has been widely reported and accepted that $Fe^{3+}$ changed into $Fe^{2+}$ when the samples were sintered in a reducing atmosphere at a high temperature. Therefore, this has to be taken into account in the study of the Fe doping effect.

# 2. Research Goals

The studies mentioned above (section 1.5.5) shed light on the understanding of the influence of Fe as a dopant in $Al_2O_3$, but there are still several fundamental questions that remain unclear:

1) In previous studies, the valence state of Fe was identified by the color of the sintered $Al_2O_3$ compact. The quantification of the ratio between $Fe^{3+}$ and $Fe^{2+}$ has never been conducted due to technical limitations.

2) Various Fe contents were added into $Al_2O_3$ without rigorously considering the Fe solubility limit in α-$Al_2O_3$, and the Fe dopant concentrations were not accurately determined inside the bulk of $Al_2O_3$ after sintering.

3) Although previous studies demonstrated the influence of Fe on densification and grain growth in $Al_2O_3$, the influence of Fe on GB mobility has not been quantitatively determined.

4) Fe segregation at $Al_2O_3$ GBs was proposed but the exact excess has not yet been quantified.

This MSc research project aims to address the above issues and the fundamental objectives are to:

1) Quantitatively study the influence of Fe on grain growth and GB mobility of $Al_2O_3$ under the condition that the dopant concentration is below the solubility limit of the sintering temperature.

2) Determine the effectivity of Fe solutes on GB migration compared with that of Mg solutes.

3) Determine the Fe valence state and study the effect of Fe valence states on $Al_2O_3$ microstructure evolution.

4) Measure Fe excess at the $Al_2O_3$ GBs and understand the mechanism by which Fe affects GB mobility.

# 3. Experimental Methods

## 3.1 Sample Processing

### 3.1.1 Slip Casting

The undoped $Al_2O_3$ (U0) green bodies were prepared using the slip-casting method. 150 g of high-purity (99.99 wt.%) α-$Al_2O_3$ powder with an average particle size of ~ 300 nm (Ceralox HPA 0.5, Tucson, AZ), 67 g of distilled water, and also 14 drops of analytically pure HCl were fully mixed for 24 h by a ball milling system without milling balls to reduce contamination from the balls. The HCl was added to deflocculate the $Al_2O_3$ suspension by adjusting the pH to approximately 4, which is well below the isoelectric point of $Al_2O_3$ (pH of 8-9) [72, 73]. The undoped $Al_2O_3$ slurry was slip cast into a Busher funnel and then was dried in two steps: (1) in a suction system until solidification; (2) in an air drying oven at ~50 ℃ for 12 h and at ~110 ℃ for 5 h.

The low Fe concentration doped $Al_2O_3$ (F1, F2) green bodies were also prepared by slip casting but with vacuum filtration. In a method identical to the undoped $Al_2O_3$ slurry preparation, the Fe-doped $Al_2O_3$ (F1 and F2) slurry was obtained by mixing 150 g $Al_2O_3$ powder, distilled water, HCl, and 28g iron (Ⅲ) nitrate nonahydrate. The added amount of distilled water in the slurries of F1 and F2 were 193 g and 75 g, respectively. After fully mixing with the same conditions, the slurries were slip cast by vacuum filtration for 2 h, and then by the same drying processes as described above.

### 3.1.2 Uniaxial Pressing

The Fe-doped $Al_2O_3$ (F3) slurry was prepared by the method mentioned above, while 115 g distilled water and 28 g high pure iron (Ⅲ) nitrate nonahydrate ($Fe(NO_3)_3 \cdot 9H_2O$) were added, followed by slip-casting and drying to obtain the green bodies. The dried green body was manually ground until the powders could go through the standard analysis sieve with 160 mesh. The final green body of F3 was compacted by uniaxial pressing at about 28 MPa.

The Mg-doped $Al_2O_3$ (M1) was prepared using a ready-to-press (RTP) $Al_2O_3$ powder (Ceralox, AHPA-0.5, Sasol North America, AZ) with a purity of 99.995 wt.%. This batch of powders contained a small amount (~300 ppm) of magnesia (MgO). The Mg-doped green bodies were prepared by uniaxial pressing at ~28 MPa.

### 3.1.3 Salt Infiltration

Due to the drawbacks of the slip-casting method, it was difficult to obtain a high Fe-level and highly dense $Al_2O_3$ sample. We also employed the salt infiltration method for the sample preparation [74]. The filtration steps are as follows and the setup is shown in Figure 12.

1) Prepare a saturated Fe solution by adding and dissolving iron nitrate in 300 ml ethanol until the sediment starts to appear.

2) Place the fired green bodies in a beaker and submerge them in the ethanol-based Fe-saturated solution.

3) Put the beaker in a desiccator connected to a vacuum pump.

4) Vacuum the desiccator system for 1 h, switch off the pump, and then keep this state for at least 5 h.

5) Take out the beaker with samples inside and dry it in a low-temperature furnace at ~ 60 ℃ for 2 h and then fire the samples at 600 ℃ for 2 h.

6) Repeat the step 2~5 for multiple times depending on the size of the sample.

To obtain the high Fe doped $Al_2O_3$ (F4) green bodies, the undoped $Al_2O_3$ green bodies were fired at 850 ℃ with 10 ℃/min for 2 h in air. They were then infiltrated with the ethanol-based Fe saturation solution for 8 cycles.

To obtain the Fe and Mg co-doped $Al_2O_3$ (FM1) green bodies, the RTP $Al_2O_3$ green bodies were infiltrated for 3 cycles.

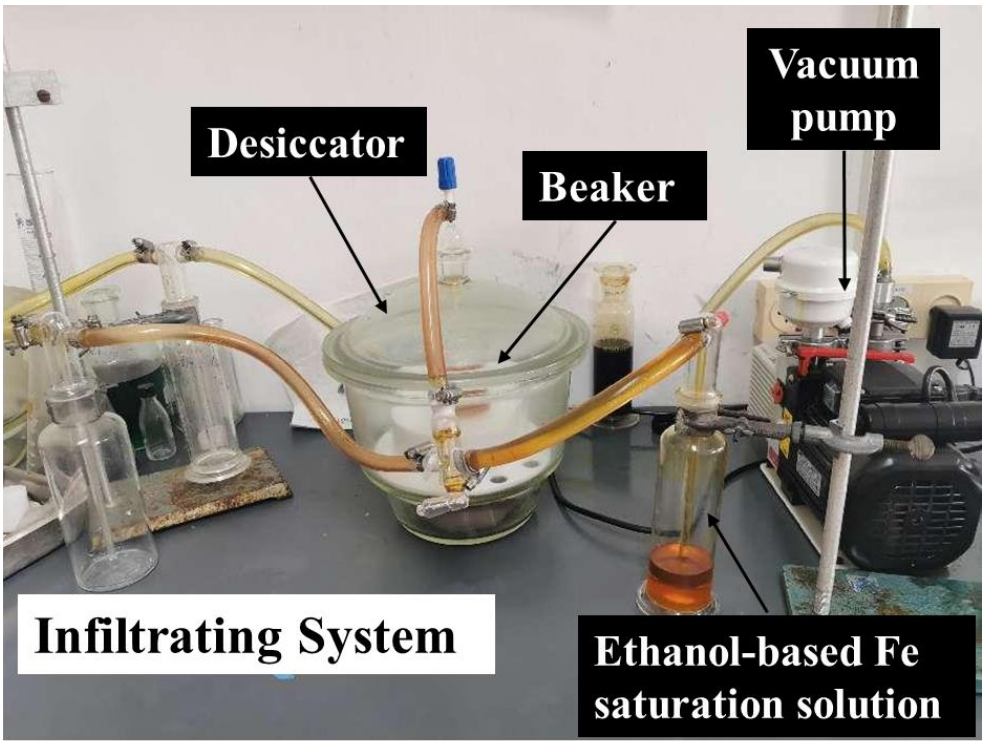


Figure 12: A photograph of the infiltration system.

The salt infiltration method introduced a heterogeneous distribution of Fe concentration but only enrichment in the surface layer (millimeter level). In the bulk, the Fe concentration was homogeneous. The surface layers were ground out.

### 3.1.4 Sintering

All green bodies prepared by slip casting, uniaxial pressing, and filtration methods mentioned above were first fired at 600 ℃ for 2 h in air. Then another 2 h firing at 1000 °C in air (heating rate 10°C/min) was conducted to promote necking formation between particles (so called bisque firing).

The final sintering was conducted at 1600 ℃ for 2 h in air with a heating and cooling rate of 10 ℃/min to achieve dense samples (relative density >95%). Muffle furnaces with different heating capacities were used in this step.

### 3.1.5 Grain Growth

After sintering the samples should be dense and the density cannot increase much. Then, we conducted the annealing process to promote grain growth for studying GB mobility. Each dense sample (U0, F1, F2, F3, F4, M1, FM1) was cut into small pieces, and then 5 of them were annealed at 1600 ℃ for different durations (1 min, 1 h, 2 h, 4 h, and 8 h) in air with a heating and cooling rate of 10 ℃/min.

## 3.2 Characterization

Systematic characterization was conducted to evaluate the relative density, chemical composition, and microstructure evolution. The relative density was measured by Archimedes' method following the ASTM standard C 20–92. X-ray diffraction (XRD) was applied to identify the phases in each sample. The Fe concentration after sintering was measured by wavelength dispersive spectrometry (WDS). A scanning electron microscope (SEM) was used to characterize the microstructure on the polished conventional cross-section of each sample. The grain size was analyzed using the linear intercept method based on SEM images. Electron backscattered diffraction (EBSD) measurements were applied to characterize the aspect ratio of anisotropic grains. The valence states of Fe were determined using X-ray photoelectron spectroscopy (XPS). Scanning transmission electron microscopy combined with energy dispersive X-ray spectrometry (STEM-EDS) was carried out to confirm and quantify the Fe excess at GBs. TEM lamellae were prepared by the focused-ion beam (FIB) lift-out technique.

### 3.2.1 Relative Density

Each sintered sample was cut into small pieces and the relative density (ρ) was measured by Archimedes' method with distilled water as the immersion medium. The operation steps were according to the ASTM standard c 20-92 [75].

$$\rho = \left(\frac{D}{W - S}\right) / \rho_{Al_2O_3} \qquad \text{Eq. (10)}$$

where $D$ represents the dry weight, $W$ represents the saturated weight, $S$ represents the suspended weight of a sample, and $\rho_{Al_2O_3}$ is the theoretical density of $Al_2O_3$ which is 3.97 g/cm$^3$.

### 3.2.2 Phase Determination by XRD

After obtaining dense samples, XRD measurements were undertaken to verify the phases present for all the undoped and doped samples. XRD patterns were acquired using an X-ray Diffractometer (Rigaku Mini Flex) with a Cu Kα rotating anode, operated at 15 mA and 40 kV. Diffraction patterns were acquired at steps of 2θ = 0.02° and with a speed of 4°/min.

### 3.2.3 Concentration Measurement by WDS

The solute concentration measurements were performed using an SEM (FEI Quanta 200 E-SEM) mounted with a WDS detector (Oxford Instruments). To optimize between high signal intensity and low background intensity, the WDS measurements were acquired at an accelerating voltage of 25 kV, a probe current of ~80 $nA$, a spot size of 8.3, a working distance of 11 mm, and a magnification of 12000x. A pure $FeS_2$ specimen was used as the standard and a lithium fluoride (LiF) crystal was used as the monochromator in the WDS measurements of Fe. The elemental $K\alpha$ peak was measured at a spectral position showing a maximum intensity. Each measurement took 20 s and over 30 measurements were taken from random locations across each polished and carbon-coated (to avoid charging) cross-section to quantify the concentration of Fe.

The WDS data was analyzed using the fully quantitative Cliff-Lorimer method [43] which is developed from the well-known Cliff-Lorimer equation in the Ref. [76, 77]. Accordingly,

$$C_{spec} = \frac{I_{spec}}{I_{std}} \cdot g_{ZAF} \cdot C_{std} \qquad \text{Eq. (11)}$$

where $C_{spec}$ is the concentration of the element, $I_{spec}$ is the intensity of characteristic X-ray radiation from the specimen. $C_{std}$ and $I_{std}$ are the element

concentration and intensity measured from the standard, respectively. $C_{std}$ is equal to 1. $g_{ZAF}$ correlates to the ZAF correction factor for atomic number (Z), absorption (A), and characteristic fluorescence (F). The XPHI software was used to calculate the $g_{ZAF}$ correction factor [78], and the $g_{ZAF}$ was 0.482.

The detection limit ($C_{lim,0.975}$) is the limit of detection with a confidence probability of 97.5% for the measurements. Taking a Poisson distribution for the background intensity, it was determined using the equation[79, 80]:

$$C_{lim.0.975} = g_{ZAF} \cdot C_{std} \cdot \frac{2\sqrt{2I_{BG}}}{\sqrt{m\tau}I_{std}} \qquad \text{Eq. (12)}$$

where $m$ is the number of measurements and $\tau$ is the single measurement time. $I_{GB}$ is the background intensity.

### 3.2.4 Grain Size Measurement Based on SEM

Cross-Section Preparation

To study the microstructure (such as pores and grains) in the bulk samples, conventional cross-section surfaces were prepared. The annealed specimens were cut using a diamond saw, and then mechanically polished using a diamond suspension with an average particle size of 1 μm on a cloth. The polished cross-sections were cleaned and were thermally etched at 1250 ℃ for 2 h in a furnace. The purpose of thermal etching was to reveal the grains by introducing GB grooving.

Micrographs Acquisition

Secondary electron SEM micrographs were obtained using a FEI Quanta 200 E-SEM, a Zeiss Ultra-Plus field emission gun SEM, and a Zeiss Gemini SEM 450.

Grain Size Analysis

Grain sizes were measured and analyzed, using a MATLAB program following the linear intercept method [79], based on the SME images containing thousands of

grains in each annealed specimen. A proportionality constant of 1.56 was used to correlate between the average grain size (in 3D) and the average intercept length (in 2D) [81]. It is worth noting that for this estimation, the grain size should follow the log-normal distribution resulting from normal grain growth.

### 3.2.5 Grain Aspect Ratio Characterization by SEM-EBSD

In order to investigate the effect of Fe dopant on the grain shape in $Al_2O_3$ and to compare the elongated degree of doped and undoped $Al_2O_3$ samples, EBSD measurements were performed on a Zeiss Gemini SEM 450 mounted with an EBSD detector (Oxford Instruments). Colloidal silica suspension was used for the final polishing. EBSD was conducted at an accelerating voltage of 20 KV, a current of 7 nA, a magnification of 500x, an acquisition step size of 0.5 μm, and on a region of interest of 200 μm × 150 μm.

### 3.2.6 Valence State Measurement by XPS

XPS is a commonly used surface analysis technique for compositional and chemical state analysis [82]. In XPS analysis, the specimen is irradiated by monochromatic X-rays, and the energy of detected electrons is analyzed. The interaction causes secondary electrons (with a limited mean free path) to be emitted by the photoelectric effect. The kinetic energies, $E_s$, of the emitted electrons can be measured [36, 82, 83]:

$$E_s = hv - E_b - \Phi \qquad \text{Eq. (13)}$$

where $hv$ is the energy of the photon, $E_b$ is the binding energy of the atomic orbital from which the electron originates, and $\phi$ is the spectrometer work function[83]. The binding energy can be regarded as the energy difference between the initial and final states after the photoelectron has left the atom [83]. Since the ions from each type of atom have a variety of possible final states, the emitted electrons have a corresponding variety of kinetic energies. Each element has its unique binding energies and variations in the elemental binding energies (also referred to as the chemical shifts) result from the differences in the chemical potential and

polarizability of compounds. Therefore, XPS can be used to identify the chemical state of the analyzed materials according to their binding energy differences arising from their chemical shifts.

XPS analyses were performed using a PHI 500 Versa Probe III. An incident monochromated X-ray beam from the Al target (15kV, 25W) was focused on a 100 μm area of the well-polished cross-section surface. The electron energy analyzer was operated with a pass energy of 224 eV. A step size of 20 eV was employed and each peak was scanned 60 times to obtain the Fe2p spectrum and 6 times to obtain spectra of other elements (Al, O, C). The sputtering technique using $Ar^+$ ion bombardment was employed to remove surface contamination [84]. The samples were $Ar^+$ sputtered for 25 min.

### 3.2.7 Grain Boundary Mobility Estimation

GB mobility estimation was carried out using grain size measurements as a function of time as reported by Powers et al. [6] and Akiva et al. [20]. Combining Eq. (1) and Eq. (4) mentioned above, the GB velocity is expressed as:

$$v_{GB} = \frac{d\bar{G}}{dt} = \frac{\alpha M_{GB}\gamma_{GB}}{\bar{G}} \qquad \text{Eq. (14)}$$

Assuming spherical grains and equiaxed growth as described in section 1.1.1, $\bar{G}$ is the average grain size, the geometric factor $\alpha$=1 and the growing part of a grain by atom diffusion is $l$, so $v_{GB} = l/t$. Then Eq. (14) can be written as:

$$M_{GB} \cdot \gamma_{GB} \cdot t = \overline{G_0} \cdot l \qquad \text{Eq. (15)}$$

where $\bar{G}_0$ *is* the initial average grain size at time t=0 before the annealing starts, $\bar{G}_0 \gg l$. The average grain size after annealing time t, $\bar{G}_t$, can be expressed as $\bar{G}_t = \bar{G}_0 + 2l$. Then,

$$\overline{G_t}^2 - \overline{G_0}^2 = 4\overline{G_0}l + 4l \approx 4\overline{G_0}l \qquad \text{Eq. (16)}$$

By substituting Eq. (15) into Eq. (16), the GB mobility estimation equation based on average grain size is expressed as:

$$\overline{G_t}^2 - \overline{G_0}^2 = 4M_{GB}\gamma_{GB}t = k \cdot t \qquad \text{Eq. (17)}$$

The $M_{GB}\gamma_{GB}$ is referred to as the *effective* GB mobility, $k$ is the rate constant and $t$ is migration time (sec). $M_{GB}\gamma_{GB} = k/4$ is a quarter of the slope of the figure (($\bar{G}_t^2 - \bar{G}_0^2$) versus time). Therefore, the GB mobility can be extracted from the grain size measurements according to the above technique. The reason for using effective GB mobility, instead of absolute GB mobility, was because of the difficulties in accurately determining the GB energy.

### 3.2.8 Quantitative Fe Excess Measurement by STEM-EDS

Analytical STEM characterization was conducted on a GB region in $Al_2O_3$ doped with 1.26 wt.% Fe. The TEM lamella sample was prepared by the focused ion beam (FIB) lift-out technique on a FIB (Thermo Fisher FIB-SEM dual-beam Helios G5). For quantitative analysis of the amount of Fe at the GB, EDS mappings were acquired in STEM (Thermo Fisher STEM Talos F200X) operated at 200 kV. A region including a GB and adjacent grains was chosen for the acquisition (see Figure 13). The amount of Fe excess at GBs in $Al_2O_3$ can estimated using Eq. (18) [20]:

$$\Gamma_{Fe} = \frac{V}{S} \cdot \rho_{Al_2O_3} \cdot k_{Fe/Al} \cdot \frac{2A_{Al}}{A_{Fe}} \cdot \frac{I_{Fe}^{excess}}{I_{Al}^{GB}} \qquad \text{Eq. (18)}$$

where $V$ is the interaction volume and $S$ is the area of the GB in the interaction volume, $\rho$ is the density of the matrix in atom/nm$^3$, $k_{Fe/Al}$ is Fe–Al k-factor correlating the intensity to concentration. $A_{Al}$ and $A_{\mathrm{Fe}}$ are the atomic masses of Al and Fe. $I_{Al}^{GB}$ and $I_{Fe}^{excess}$ are the measured characteristic X-ray intensities of the Al in GB area and excess Fe in GB area in EDS spectra, respectively.

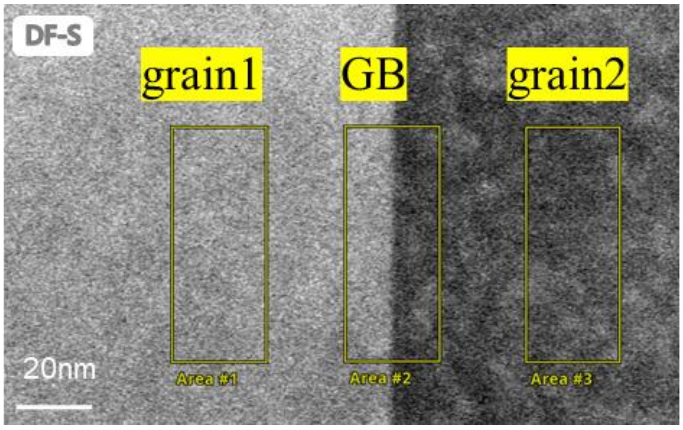


Figure 13: Dark field STEM of a GB in a sample, demonstrating the regions scanned for EDS measurements of the GB excess. The selected areas for measurements are indicated in yellow boxes.

The excess Fe elemental intensity at the GB area is determined using the STEM spatial difference technique according to Ref. [85] as:

$$I_{Fe}^{excess} = I_{Fe}^{GB} - 0.5I_{Fe}^{grain1} - 0.5I_{Fe}^{grain2} \qquad \text{Eq. (19)}$$

The detection limit of this measurement was determined by [20]:

$$\Gamma_{min} = \frac{V}{S} \cdot \rho_{Al_2O_3} \cdot k_{Fe/Al} \cdot \frac{2A_{Al}}{A_{Fe}} \cdot 3 \cdot \frac{\sqrt{2I_{Fe}^{b}}}{I_{Al}^{GB}} \qquad \text{Eq. (20)}$$

where $I_{Fe}^{b}$ is the intensity in the background under the elemental peak of Fe.

The k-factor ($k_{Fe/Al}$) was experimentally determined using the Cliff-Lorimer technique [77]. A standard Fe-doped $Al_2O_3$, in which the Fe concentration was accurately known, was employed for the measurement.

$$\frac{C_{Fe}}{C_{Al_2O_3}} = k_{Fe/Al} \times \frac{I_{Fe}}{I_{Al_2O_3}} \qquad \text{Eq. (21)}$$

where $C_{Fe}$ and $C_{Al_2O_3}$ are the weight percentage of each element, in which $C_{Fe} + C_{Al_2O_3}$=1.

# 4. Results

## 4.1 Relative Density and Dopant Concentration

The measured average relative density and the actual solute concentration of sintered samples are presented in Table 2. All the samples are dense, and their relative densities are higher than 95% which means there are only closed pores in the samples. Since different methods were applied for sample preparation, various Fe concentration doped $Al_2O_3$ and Mg-doped $Al_2O_3$ samples were obtained. The solute concentrations changed from 0 to 3 wt.% and were all below the solubility limit. The measured WDS detection limit of Fe in $Al_2O_3$ is $2.7\times10^{-5}$ wt.%, which is far below the results of dopant concentration detection. This ensured the measurements were reliable.

Table 2: The average relative density and actual dopant concentration of samples.

| Sample | Relative Density | Actual Dopant Concentration |
|---|---|---|
| **U0** | 98.7% | / |
| **F1** | 97.0% | 0.18 wt.%(Fe) |
| **F2** | 97.9% | 0.71 wt.% (Fe) |
| **F3** | 96.5% | 1.26 wt.% (Fe) |
| **F4** | 98.6% | 2.93 wt.% (Fe) |
| **M1** | 98.0% | ~0.01 wt.% (Mg) |
| **FM1** | 96.7% | ~0.01 wt.% (Mg) and 0.41 wt.%(Fe) |

## 4.2 XRD Results

XRD data of undoped and doped samples is presented in Figure 14. The XRD patterns present only α $Al_2O_3$ peaks and no detectable secondary phases, as expected. The results also corroborated that the concentrations of Fe and Mg were below the solubility limit.

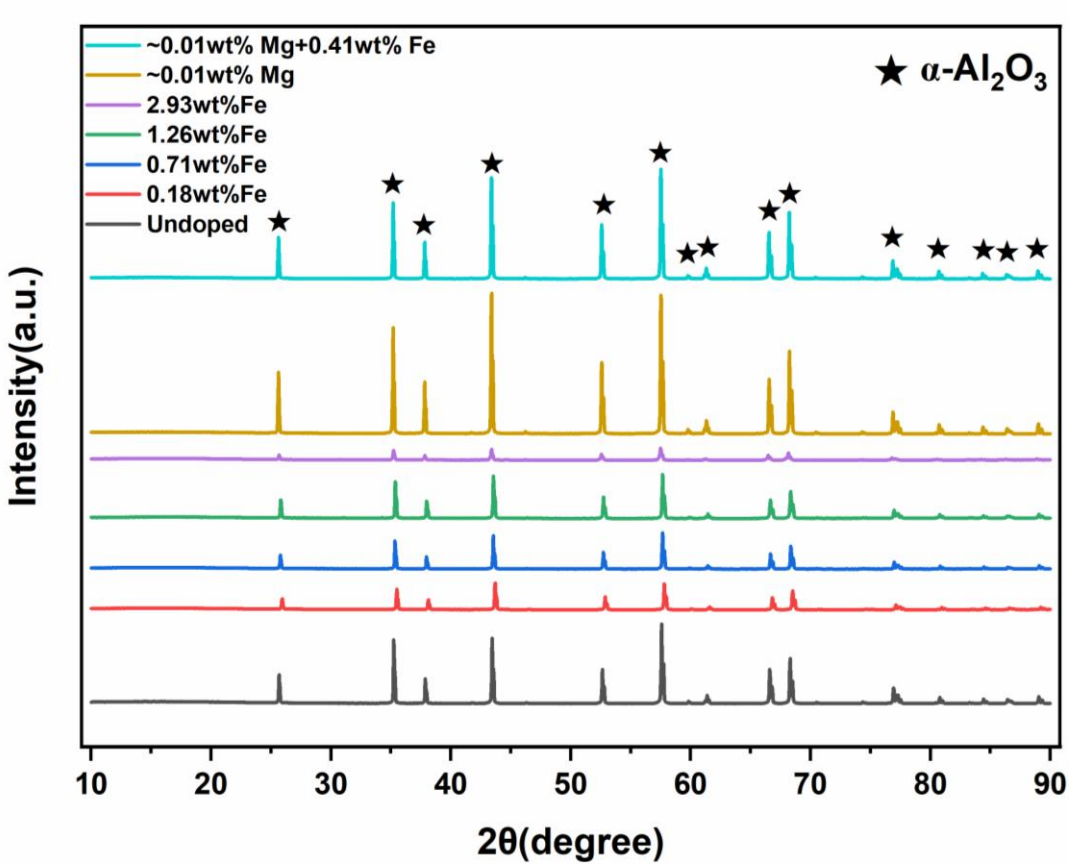


Figure 14: XRD patterns from the undoped $Al_2O_3$ sample and doped $Al_2O_3$ samples with different dopant concentrations, sintered at 1600 °C for 2 h in air. Reflections from second phases were not detected.

## 4.3 Valence State of Fe Dopant

Charge Calibration

The detected Fe2p spectrum was charge calibrated using the Al2p peak measured in the same test on the same sample since Al is also a metal element and more stable than other nonmetal elements (C and O). The measured peak position of Al2p was

at 74.2 eV while the standard peak position of Al2p is at 74.4 eV [83]. The C1s peak was often employed as the reference for charge correction in many studies. However, the position of the C1s peak was reported to be steered by the sample work function as in Refs. [82, 86] and it cannot be chosen to serve as a reliable reference peak for calibrating the binding energy scale in the present studies.

Peak Fitting and Results

Much of the key information of XPS results is based on peak fitting which is an indispensable part of XPS data analysis [87]. The corrected Fe2p spectrum was fitted using a series of multiplet patterns using software (XPS PEAK41) based on the properties of each pure Fe valence state, such as peak positions (main peaks: $Fe2p_{1/2}$ and $Fe2p_{3/2}$) of valence states, full width at half maximum (FWHM), modified Shirley background, and satellite peaks [88-90]. Fe2p spectral fitting was based on the related parameters of standard spectra of Fe(II) and Fe(III) [83, 86, 89].

Figure 15 presents the optimal curve fitting of the Fe2p spectrum obtained from the 2.93 wt.% Fe-doped $Al_2O_3$ sample given the $Fe2p_{3/2}$ peak position of 709.60 eV for Fe(II) and 710.95 eV for Fe(III), respectively. The resulting fit suggests a mix of trivalent Fe and divalent Fe components. The fitting was assessed by the goodness of fit i.e. the minimum $\Sigma\chi^2$=0.3349. The ratio between Fe(III) and Fe(II) content was 1.86 estimated by the ratio of area intensities of main peaks. The fit parameters are listed in Table 3.

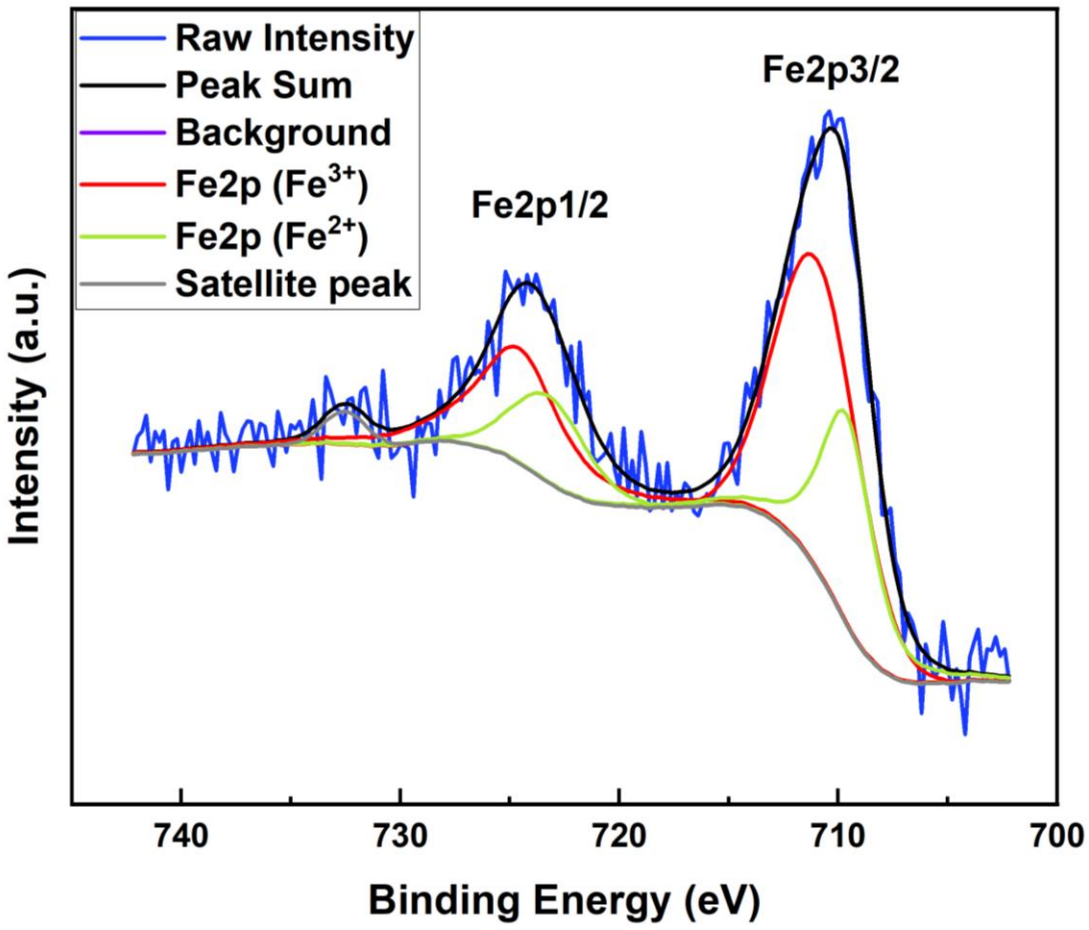


Figure 15: The fitted XPS spectrum of Fe2p from the polished cross-section of the 2.93 wt.% Fe-doped $Al_2O_3$ sample.

Table 3: Fe2p spectral fitting parameters: peak position (eV), peak area, FWHM value (eV), and Gaussian–Lorentzian ratio (%GL) (eV).

| Peak | Position (eV) | Area | FWHM (eV) | %GL |
|---|---|---|---|---|
| **Fe(III) $2p_{3/2}$** | 710.950 | 5609.589 | 4.469 | 1 |
| **Fe(III) $2p_{1/2}$** | 724.550 | 2804.795 | 4.398 | 80 |
| **Fe(II) $2p_{3/2}$** | 709.600 | 3014.509 | 2.805 | 57 |
| **Fe(II) $2p_{1/2}$** | 723.200 | 1507.254 | 3.966 | 19 |
| **satellite peak** | 732.542 | 294.907 | 2.245 | 0 |

Since the Fe contents in other samples are too low to be detected in XPS, only the highest Fe-doped sample (in the same sintering condition) was used. From this, it

was assumed that all the Fe-doped samples include two Fe valence states ($Fe^{3+}$ and $Fe^{2+}$) but with different ratios.

## 4.4 Microstructure and Grain Growth

Micrographs

The microstructures of the undoped and doped $Al_2O_3$ annealed for 2 h at 1600 °C in air are shown in Figure 16. According to the figure, even though the samples were dense, there were still some closed pores in the grain interiors, on the GBs, and at the triple junctions. Some of the pores were caused by the pull-out introduced during the mechanical polishing process to prepare the SEM samples. Figure 16 indicates that the average grain size decreases with an increase in Fe concentration. In addition, grains in the $Al_2O_3$ specimen with the highest Fe concentration (2.93 wt.%) exhibited an elongated morphology while the grains in other samples showed an equiaxed morphology. Tartaj et al. [65] also found lath-shaped grains in α-$Fe_2O_3$-doped $Al_2O_3$. In order to quantify the anisotropic degree of grains, EBSD characterization was performed.

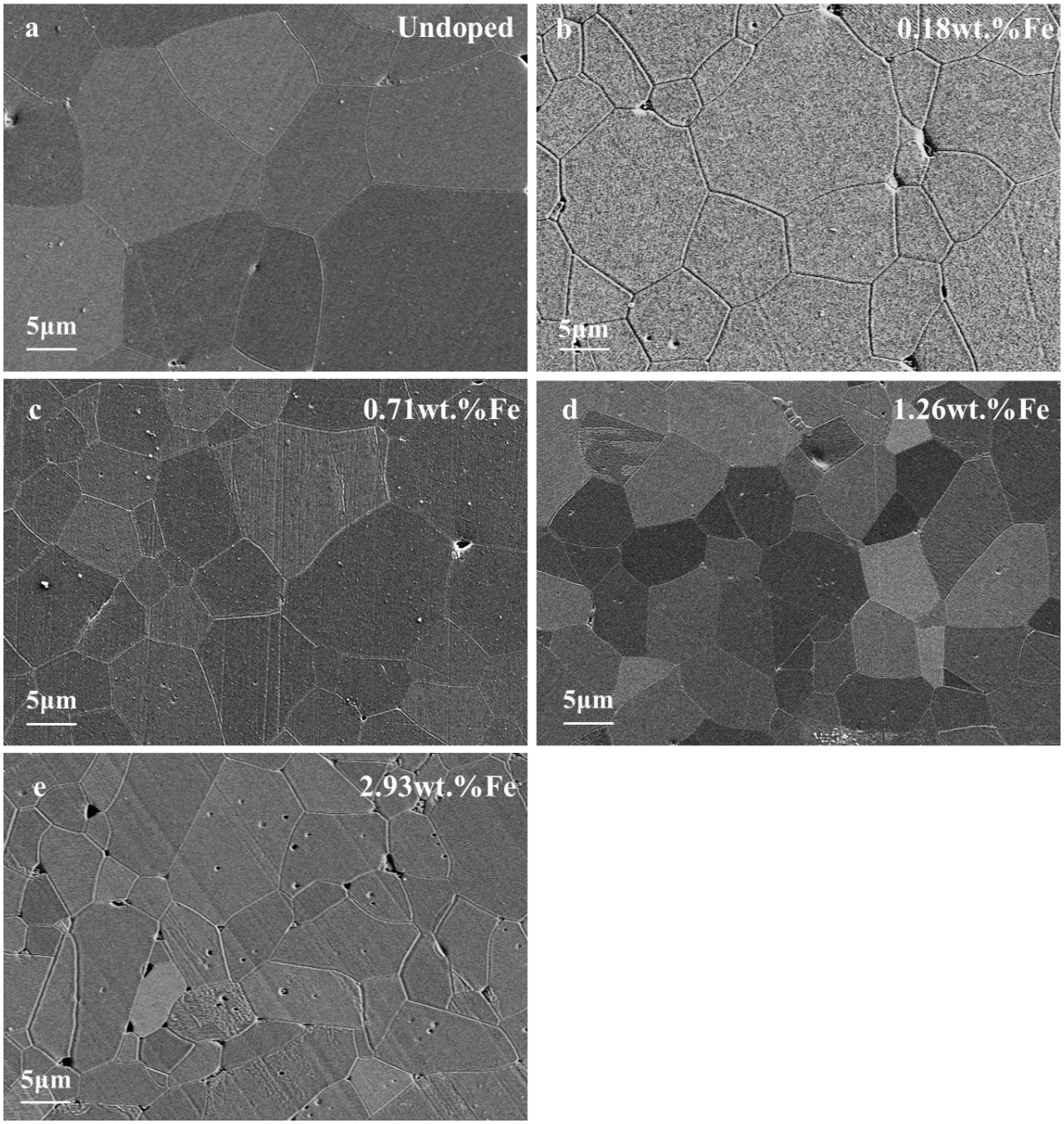


Figure 16: Secondary electron SEM micrographs (polished cross-section) of the microstructure of (a) undoped $Al_2O_3$, (b) 0.18 wt.% Fe-doped $Al_2O_3$, (c) 0.71 w.t% Fe-doped $Al_2O_3$, (d) 1.26 wt.% Fe-doped $Al_2O_3$, (e) 2.93 wt.% Fe-doped $Al_2O_3$ annealed for 2 h at 1600 °C in air.

## Aspect Ratio

The band contrast (BC) maps and inverse pole figure (IPF) micrographs obtained from EBSD measurements of undoped, 1.26 wt.% Fe-doped and 2.93 wt.% Fe-doped $Al_2O_3$ with a hit rate higher than 93% are shown in Figure 17. After the

analysis, the obtained aspect ratio of more than 1000 grains (by excluding the corner and edge grains) is shown in Table 4. It was found that the aspect ratio of 2.93 wt.% Fe-doped $Al_2O_3$ was higher than that of 1.26 wt.% Fe-doped and undoped $Al_2O_3$. This quantitative analysis clearly demonstrated that the sample with the highest Fe content contained elongated grains. The existence of different valence states of Fe, including both Fe(II) and Fe(III), may contribute to the formation of the anisotropic microstructure.

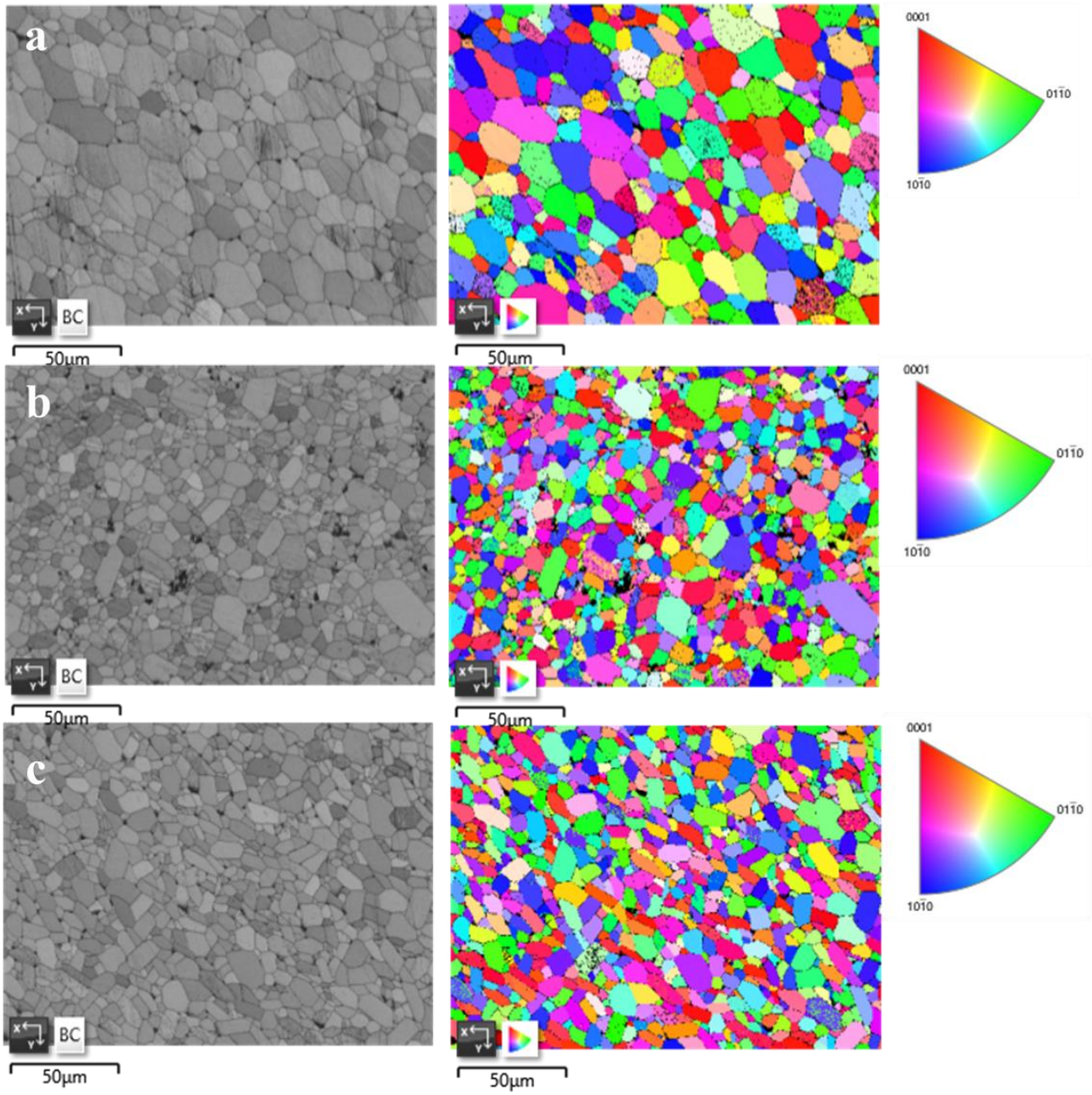

Figure 17: EBSD BC maps and IPF micrographs of undoped (a), 1.26 wt.% Fe-doped (b) and 2.93 wt.% Fe doped (c) samples annealed at 1600 ℃ for 2 h in air. The indexed rates are higher than 93%.

Table 4: The measured aspect ratio of 1.26 wt.% Fe-doped $Al_2O_3$ and 2.93 wt.% Fe-doped $Al_2O_3$ annealed at 1600 ℃ for 2h in air.

| **Sample** | **Aspect Ratio** |
|---|---|
| **undoped $Al_2O_3$** | 1.57 ± 0.16 |
| **1.26 wt.% Fe doped $Al_2O_3$** | 1.56 ± 0.21 |
| **2.93 wt.% Fe doped $Al_2O_3$** | 1.81 ± 0.33 |

Grain growth

Figure 18 demonstrates the change of the grain size in a dense sample after annealing after 1 min and 4 h. Since the 2.93 wt.% Fe-doped $Al_2O_3$ exhibited a strong anisotropic microstructure, the method of measuring grain size and GB mobility cannot be applied. The grain size distributions in other samples annealed at 1600 ℃ in air were elaborated and plotted as a function of the annealing time as shown in Figure 19. It indicated that doping Fe hindered grain growth and the grain size decreased with the increase in Fe concentration when the concentrations were below the solubility limit.

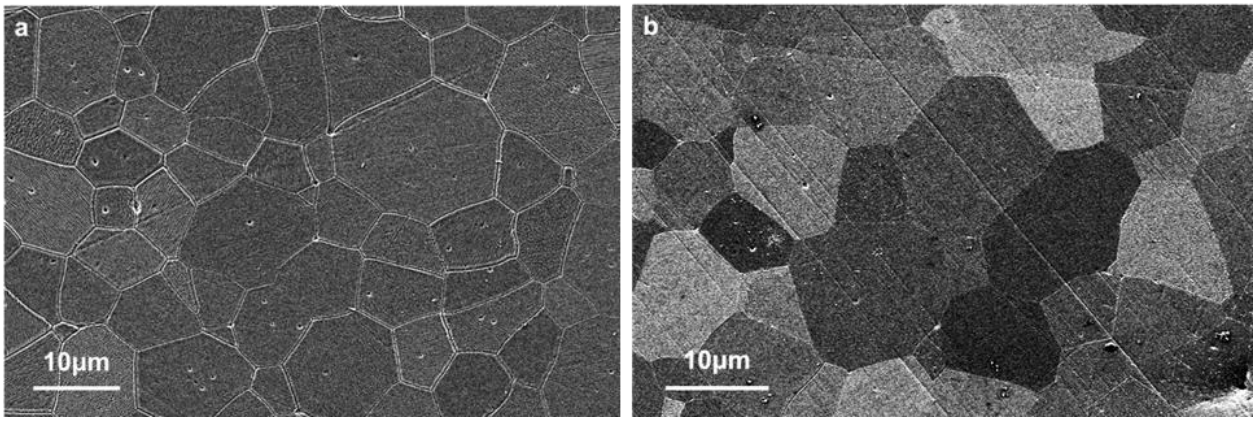


Figure 18: Secondary electron SEM micrographs (on polished cross-sections) of the microstructure of Fe-doped $Al_2O_3$ (0.71 wt.%) annealed for (a) 1 min and (b) 4 h at 1600 °C in air.

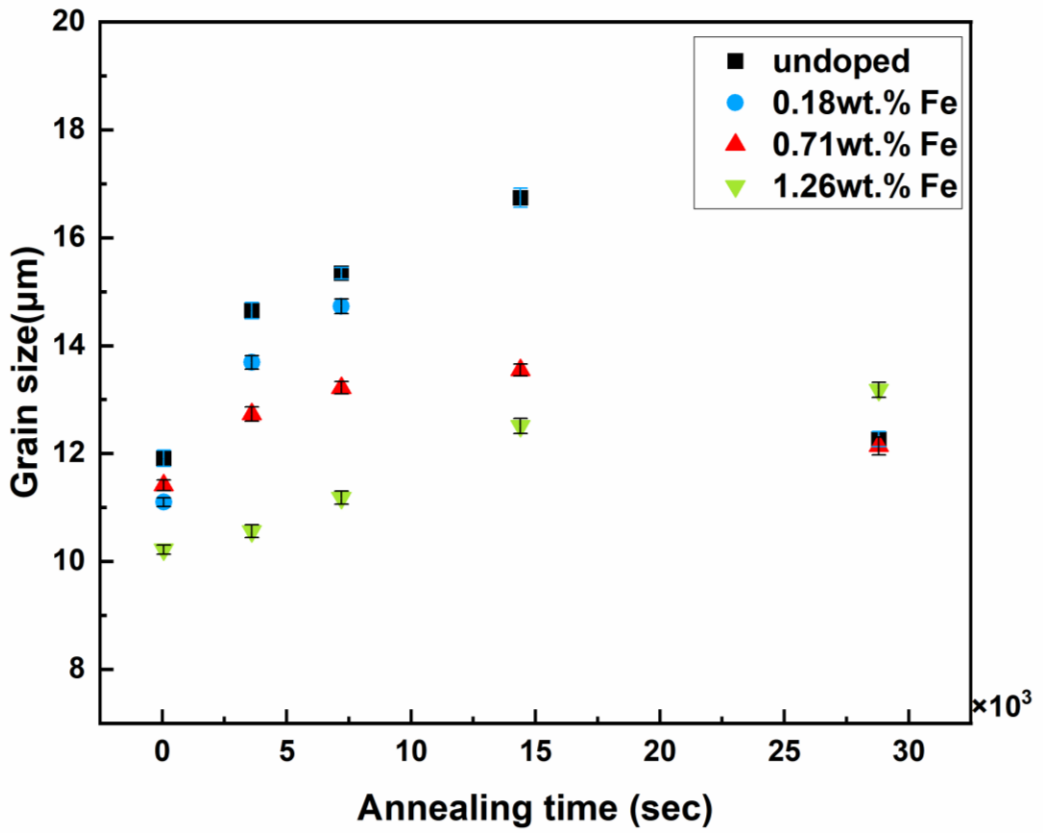


Figure 19: Grain size of undoped $Al_2O_3$ and $Al_2O_3$ doped with various concentrations of Fe (0.18 wt.%, 0.71 wt.%, 1.26 wt.%) after different annealing durations at 1600 °C in air.

As seen in Figure 20, the grain size of the Mg-doped $Al_2O_3$ samples was also smaller than that of the undoped $Al_2O_3$, which is consistent with the conclusions in Refs. [22, 49]. It is also worth noting that the concentration of Mg (~0.01 wt.%) was much smaller than that of Fe (1.26 wt.%) but the former contributed to a stronger drag effect. Finally, the Mg and Fe co-doped $Al_2O_3$ exhibited the smallest grains as a result of the drag effect from both dopants.

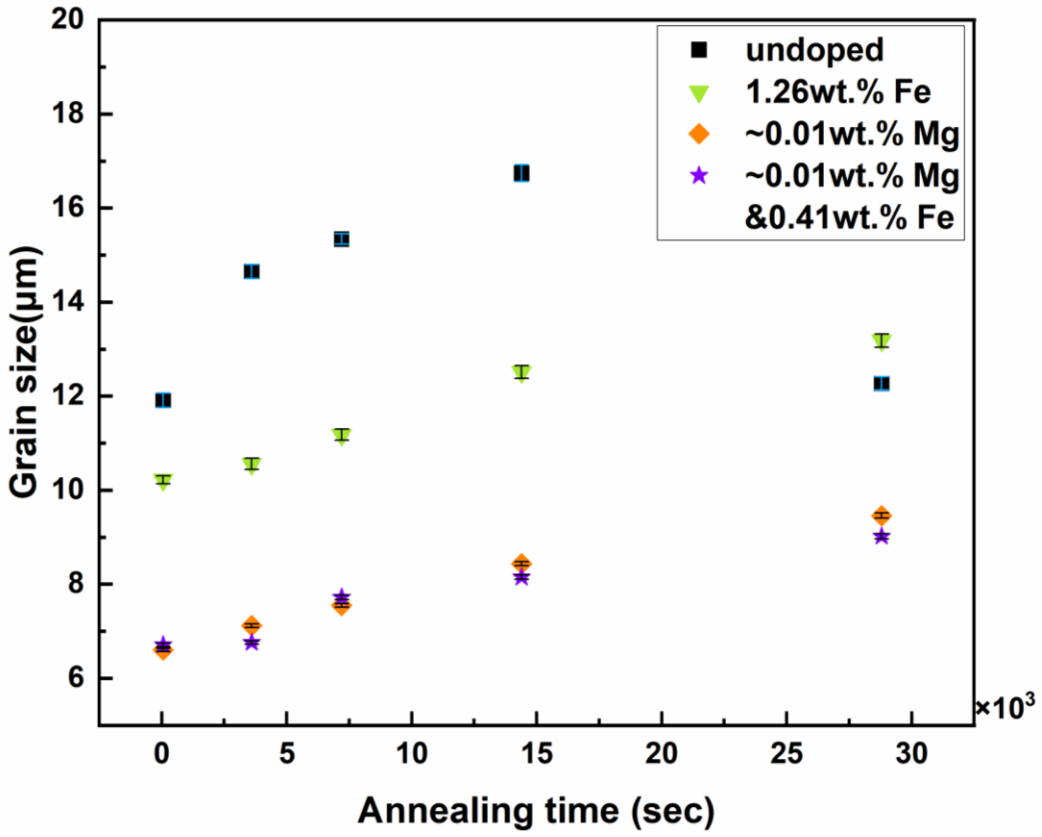


Figure 20: Grain size comparison of undoped, 1.26 wt.% Fe-doped, ~0.01 wt.% Mg-doped, and ~0.01 wt.% Mg and 0.41 wt.% Fe co-doped $Al_2O_3$ after different annealing durations at 1600 °C in air.

## 4.5 Effective Grain Boundary Mobility

Fe Concentration vs. Effective GB Mobility

The effective GB mobility was determined from the parabolic grain growth kinetics according to Eq. (17). The GB mobilities of the undoped and doped $Al_2O_3$ with various Fe concentrations are plotted in Figure 21. It is worth noting that the GB mobility was determined using the grain sizes from the early stages of growth so as to eliminate the influence of the plateau of grain size. The slopes of the fittings represent the values of the effective GB mobility. The effective GB mobility ($M_{1min}$) of the sample annealed for 1 min was set as the initial growth stage, i.e. $M_{1min}=0$. Compared to undoped $Al_2O_3$, the effective GB mobility of 0.18 wt.% Fe-doped $Al_2O_3$ was nearly identical, indicating a minor drag effect from a low concentration of Fe. Moreover, with a higher Fe concentration, the effective GB mobility decreased.

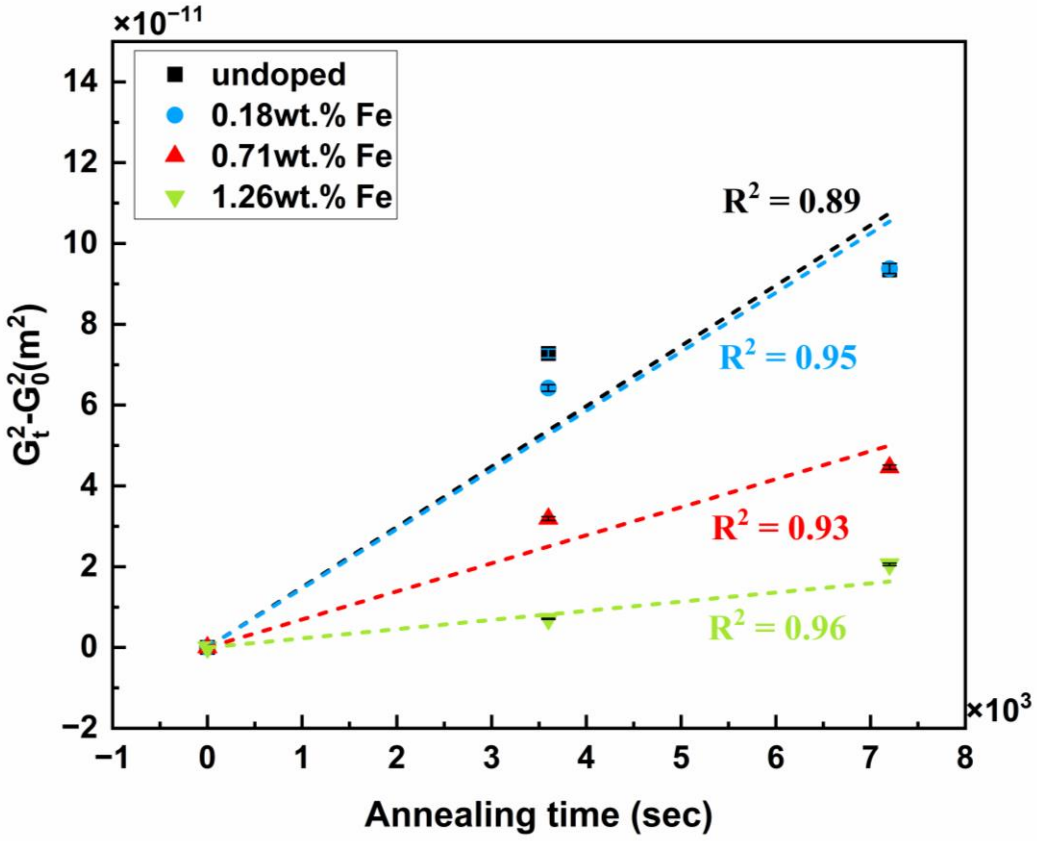


Figure 21: Grain growth kinetics of undoped $Al_2O_3$ and $Al_2O_3$ doped with various concentrations of Fe. The slopes represent the values of the effective mobility of the different samples. The goodness of fit is shown as $R^2$-values. Grain growth kinetics of the sample annealed for 1 min was the setting as the initial site $M_{1min}$=0.

## Different Dopant Species vs. Effective GB Mobility

The grain growth kinetics of undoped, various Fe contents doped, Mg-doped, and Mg-Fe co-doped $Al_2O_3$ annealed at 1600 ℃ in air are presented in Figure 22, and the calculated effective GB mobilities of samples are summarized in Table 5. The results show that both Fe and Mg dopants hinder GB motion. Also, 0.01 wt.% Mg-doped $Al_2O_3$ had smaller effective GB mobility ($3.2 \times 10^{-16}$ $m^2$/sec) than that of 1.26 wt.% Fe-doped $Al_2O_3$ ($4.1 \times 10^{-16}$ $m^2$/sec) which means Mg contributes to a stronger effect than Fe on retarding GB migration.

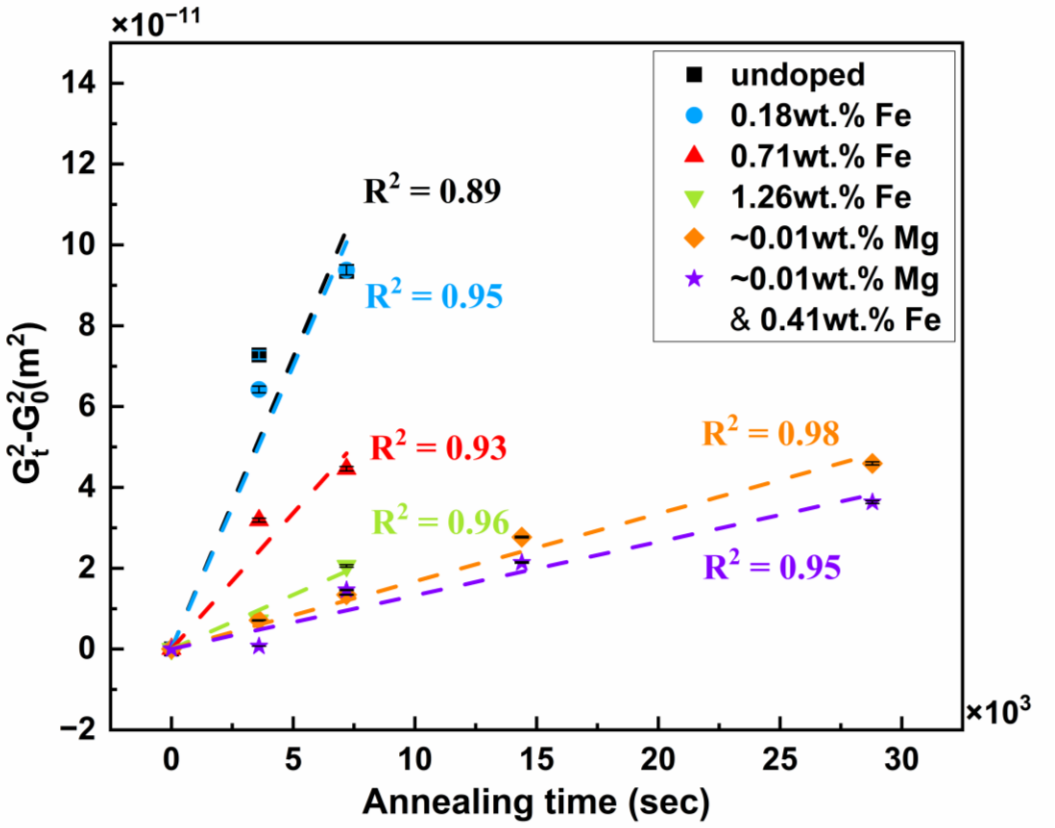


Figure 22: Summary of grain growth kinetic of undoped, various Fe contents doped, Mg-doped and Mg-Fe co-doped $Al_2O_3$ annealed at 1600 °C in air for different durations. The goodness of fit is shown as $R^2$-values.

Table 5: Effective grain boundary mobility of all tested samples.

| Samples | Dopant Concentration | Effective Mobility [$10^{-15}$ $m^2$/sec] |
|---|---|---|
| **U1** | undoped | $2.80 \pm 0.66$ |
| **F1** | 0.18 wt.%(Fe) | $2.60 \pm 0.44$ |
| **F2** | 0.71 wt.% (Fe) | $1.27 \pm 0.24$ |
| **F3** | 1.26 wt.% (Fe) | $0.41 \pm 0.08$ |
| **M1** | ~0.01 wt.% (Mg) | $0.32 \pm 0.02$ |
| **FM1** | ~0.01 wt.% (Mg) and 0.41 wt.%(Fe) | $0.25 \pm 0.10$ |

## 4.6 Excess of Fe at Grain Boundaries

Selected GB regions are presented in Figure 23. Since the GB is a relatively less dense structure compared to grains, a curtaining effect may be generated during ion milling, resulting in a local change in thickness. The curtaining effect is created by spatial variation of the sputter rate of the specimen during FIB thinning. To reduce the curtaining effect, GBs perpendicular to the FIB thinning direction (see Figure 23a) were selected for analysis. The $k_{Fe/Al}$ factor measurement was conducted on a region of 456 nm × 482 nm in 1.26 wt.% Fe-doped sample. Five measurements were performed and the average value of $k_{Fe/Al}$ was determined to be 0.60. EDS maps were acquired from the selected areas marked in yellow in Figure 23b. The area of each EDS analysis was chosen to be 50 nm × 74 nm. As shown in Figure 23b, area #1 is in grain No.1 and area #3 is in grain No.2. Area #2 is between the two grains and contains the GB. Representative EDS spectra from the three areas are shown in Figure 24.

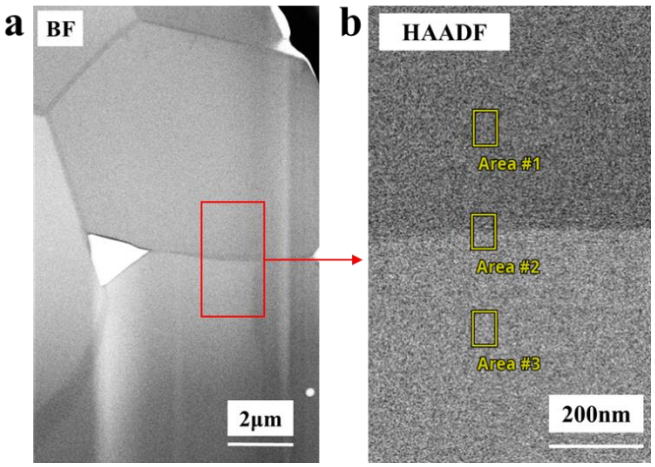


Figure 23: (a) BF-STEM micrograph demonstrating the GB chosen for the EDS analysis. (b) HAADF-STEM micrograph showing three selected regions for EDS analysis using the spatial difference method.

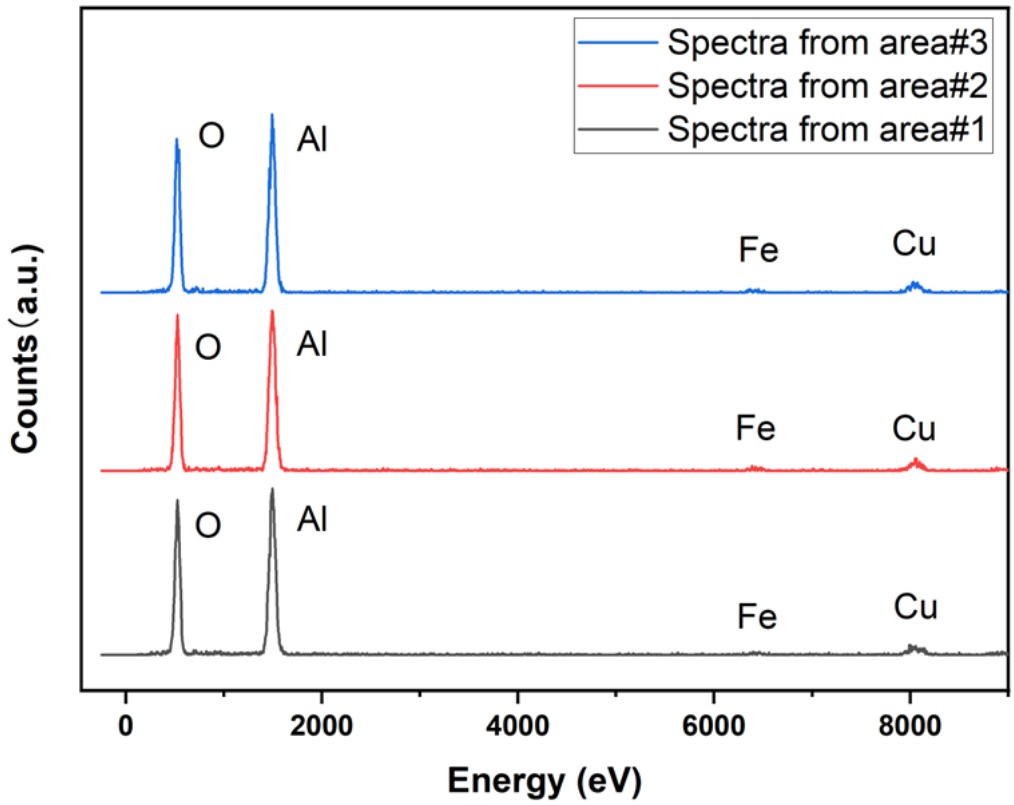


Figure 24: EDS spectra acquired from the interface region shown in Figure 23b. The spectrum from area#1 in grain No.1 adjacent to the GB is marked in gray; The spectrum acquired from area#2 including grain boundary is marked in red; and the spectrum from area#3 in grain No.2 adjacent to the GB is marked in blue. The Cu signal is from the TEM grid upon which the sample was mounted.

The EDS spectra were acquired in STEM mode using the spatial difference method. After five measurements and calculations, the excess of Fe elements at the specific GB in the $Al_2O_3$ sample with 1.26 wt.% Fe was determined to be 3.6±1.4 Fe atoms/nm$^2$, with a detection limit of 1.8±0.6 Fe atoms/nm$^2$. To the best of our knowledge, this was the first attempt at quantifying the Fe excess at $Al_2O_3$ GBs. These values seem reasonable as previous studies demonstrated that the Ca excess at $Al_2O_3$ GBs was measured to be 2.5 Ca atoms/nm$^2$ and 6.1 Ca atoms/nm$^2$ (samples contain Ca above the solubility limit) [20, 91]. Our result of Fe excess certainly confirmed that Fe dopants could segregate to $Al_2O_3$ GBs.

# 5. Discussion

## 5.1 The Influence of Fe Valence State on The Microstructure Evolution

It has been reported that $Fe^{3+}$ changes to $Fe^{2+}$ in a low $pO_2$ atmosphere or a reducing condition. In addition, the matrix composition and treatment temperature can also significantly affect the decomposition sequence of the $Fe(NO_3)_3 \cdot 9H_2O$, which determines the valance state of Fe ions. Shaheen et al. studied the thermal behavior of high-purity $Fe(NO_3)_3$ and revealed that it decomposed to $Fe_2O_3$ at 250 ℃ and was thermally stable up to 1000 ℃ [92]. Gadalla et al. also made the same discovery when they investigated the thermal decomposition of Fe(III) nitrate in stagnant or flowing air with a heating rate of 1℃/min [93]. It is of the utmost importance that the change in $Fe^{3+}$ and $Fe^{2+}$ in air was experimentally identified in their work. The decomposition of $Fe_2O_3$ occurred to be a magnetite ($Fe_3O_{4+x}$) in the temperature range of 1372 ℃-1400 ℃ when it was heated up to 1500 ℃. The phase diagram of the FeO-$Fe_2O_3$ system (see Figure 25) confirms the decomposition of $Fe_2O_3$ in air to nonstoichiometric magnetite (rich in oxygen, $Fe_3O_{4.09}$ at 1400 °C) [2, 93]. Therefore, $Fe^{3+}$ may partially change into $Fe^{2+}$ in a Fe-$Al_2O_3$ system at high temperatures in air.

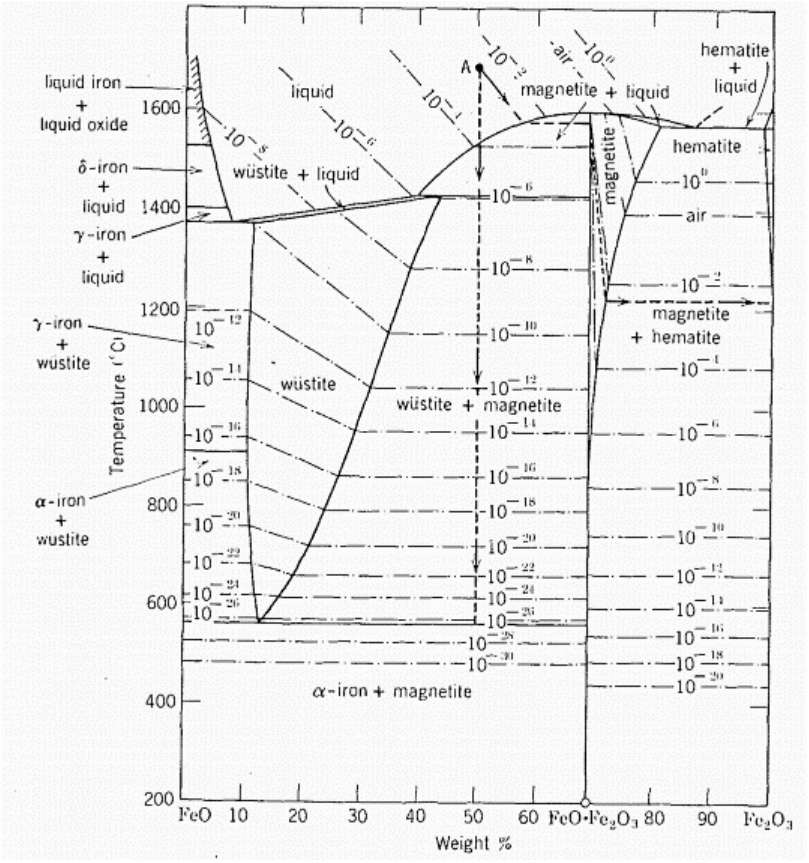


Figure 25: Phase diagram of the FeO-$Fe_2O_3$ system. Dash-dot lines are oxygen isobars [2].

In this study, doped specimens were prepared using $Fe^{3+}$ as the initial dopant and were sintered in air at 1600 °C. The sample appearance changed in color due to sintering as seen in Figure 26. The colors of the specimens are similar to those in Tartaj et al.'s work [65] which were green after sintering. Different colors may indicate changes in the valence states of Fe. However, distinguishing the Fe valence states from color is not a rigorous approach. To the best of our knowledge, the valence states of Fe in the α $Al_2O_3$ system after sintering have not been experimentally identified in the past. In this work, the XPS results confirmed that the specimen contained two valence states ($Fe^{3+}$ and $Fe^{2+}$) after sintering. Moreover, the $Fe^{3+}$ ion content is ~1.86 times the content of $Fe^{2+}$ ions based on the intensity ratio of peaks in the Fe2p XPS spectra.

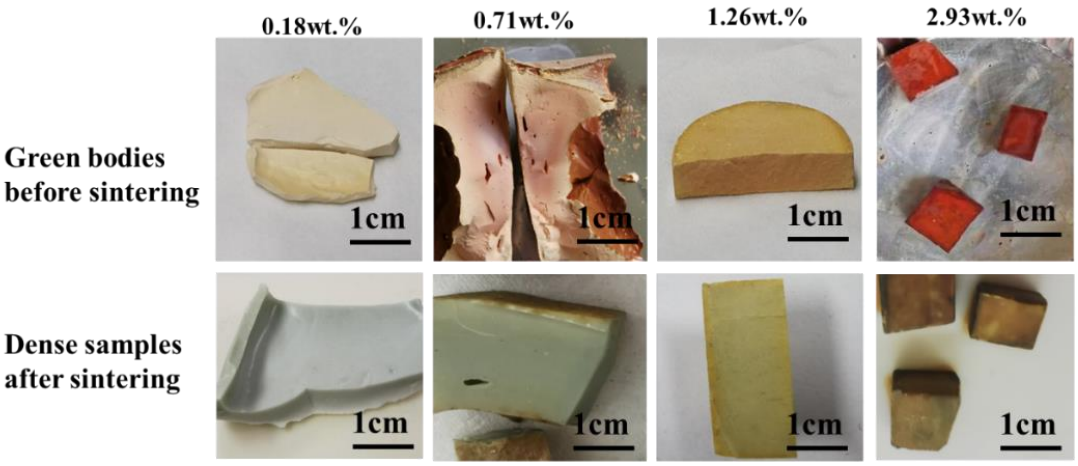


Figure 26: Green bodies and sintered dense specimens demonstrating the color change due to the evolution of the valance state of Fe dopant.

From the micrograph (Figure 16), anisotropic grain growth was observed in 2.93 wt.% Fe-doped $Al_2O_3$. Compared with undoped $Al_2O_3$, morphology analysis showed an increase in the aspect ratio in Fe-doped $Al_2O_3$. The solutes' segregation to GBs influences their migration and thus affects the grain growth. The fundamental explanation of anisotropic grain growth in Tartaj's work is attributed to the presence of $Fe^{2+}$, which was thought to significantly improve mass transport [65]. In our work, both $Fe^{3+}$ and $Fe^{2+}$ were identified in the specimen with an anisotropic microstructure. Hence three hypotheses associated with the valence state of Fe dopants can be proposed:

**i** One Fe valence state *accelerates* GB motion while the other *hinders* GB motion.

**ii** Both valence states *accelerate* GB movement but with different velocities.

**iii** Both valence states *hinder* GB migration but with different velocities.

Through experimental measurement and estimation of the effect of Fe (mainly trivalent Fe) on normal grain growth in $Al_2O_3$, it was demonstrated that Fe dopants, with a concentration below the solubility limit, exhibit a solute drag effect on GB mobility and grain growth. The level of retardation increases with an increasing Fe concentration as shown in Figure 20: and Figure 21 (more details will be given in the next two sections). Hence hypothesis ***ii*** is invalid. In addition, as mentioned in

section 1.5.5, $Fe^{2+}$ (in the form of FeO) was found to promote grain growth, and anisotropic grain growth was discovered after sintering in a reducing condition which reduced $Fe^{3+}$ to $Fe^{2+}$. Therefore, hypothesis ***iii*** can be excluded. Therefore, it can be concluded that hypothesis ***i*** "$Fe^{2+}$ accelerates GB motion while $Fe^{3+}$ hinders GB motion" could be the mechanism for anisotropic grain growth.

In this work, the anisotropic grains were mostly presented in 2.93 wt.% Fe-doped $Al_2O_3$ with ($c(Fe^{3+})/c(Fe^{2+})$ = 1.86 from XPS measurements), showing a relationship between anisotropy and concentration and valence states. The Fe dopants were characterized by STEM-EDS to confirm segregation at GB regions. The Fe excess at the GB is identified to be 3.6±1.4 Fe atoms/$nm^2$. The hypothesis ***i*** may be detailed in that $Fe^{3+}$ and $Fe^{2+}$ segregate to different GBs in one grain resulting in different migration velocities. $Fe^{3+}$ preferential segregation results in low-mobility GBs while $Fe^{2+}$ preferential segregation results in high-mobility GBs. This is briefly illustrated in Figure 27.

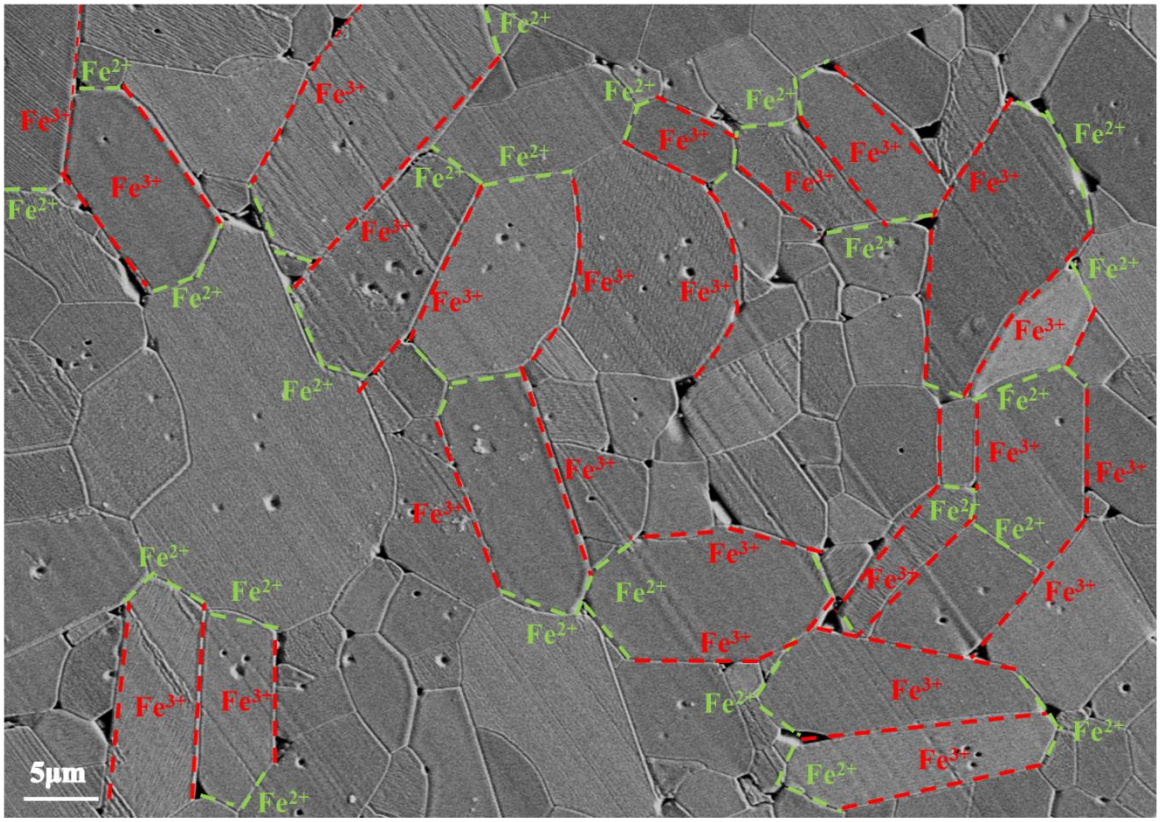


Figure 27: Secondary electron SEM of anisotropic microstructure with superimposed dashed lines demonstrating the segregation of $Fe^{3+}$ and $Fe^{2+}$ on GBs. GBs controlled mainly by $Fe^{3+}$ and $Fe^{2+}$ segregation are highlighted in the red and green dashed lines, respectively. This is the 2.93 wt.% Fe-doped $Al_2O_3$ sample annealed at 1600 °C for 2 h in air.

## 5.2 The Influence of Fe on Grain Growth

According to the micrographs (Figure 16), relatively high contents of Fe doping resulted in anisotropic grain growth. Based on the last discussion section, it can be proposed that the generation of anisotropic grain growth (sintering in air) is associated with Fe concentration, specifically the ratio of $Fe^{3+}$ and $Fe^{2+}$. However, Fe dopants with relatively low concentration levels do not significantly affect the grain shape in $Al_2O_3$, but distinctly inhibit grain growth.

This study experimentally investigated the influence of Fe dopants on grain growth. After analyzing the grain size of fully dense $Al_2O_3$ samples doped with various Fe contents (0 wt.%, 0.18 wt.%, 0.71 wt.%, and 1.26 wt.%) below the solubility limit,

Fe was found to retard grain growth and this increases with increasing Fe concentration (Figure 19). The Fe cations may be mostly or all in the $Fe^{3+}$ state, and few or none in the $Fe^{2+}$ state, since $Fe^{3+}$ is the original dopant. Therefore, it is reasonable to assume that the drag effect on grain growth is owed to the existence of $Fe^{3+}$ ions. Drahus et al. [66] also found the same effect on grain growth in 1000 ppm Fe doped $Al_2O_3$ sintered at 1350 ℃ in air, using the same grain size analysis methods.

Other dopant species, such as Mg and Cr [94], also inhibit grain growth. Especially Mg, at concentrations below and above the solubility limit, was widely reported to limit grain growth [2, 6, 21, 48, 52, 95]. As stated above, in the present study a comparison of grain growth in 1.26 wt.% Fe, ~0.01 wt.% Mg and 0.41 wt.% Fe + 0.01 wt.% Mg co-doped $Al_2O_3$ demonstrated that Mg has a stronger effect on hindering grain growth than that of Fe (Figure 20).

Solute drag has been used to explain the mechanism by which dopants and /or impurities hinder grain growth to help control the microstructure of polycrystalline materials. It is accepted that MgO hinders grain growth by introducing solute drag (or impurity drag) [48]. Solute segregation to GBs is to be expected for solute drag to occur. Fe (at a concentration below the solubility limit) was found to be enriched at a GB, and Fe solutes mainly present in a trivalent state, had a drag effect on grain growth in the present work. Hence solute drag as the possible mechanism is proposed. The difference in drag effectivity originated from the dopant itself, which may relate to the charge, atomic size, and induced defect types.

## 5.3 The Influence of Fe on Grain Boundary Mobility

The GB mobility was studied after annealing on the fully dense specimens thus the influence of Fe on densification and the drag from pores can be neglected. The effective mobility data in Table 5 clearly shows that Fe as a dopant (at a level below the solubility limit) decreases the effective GB mobility of $Al_2O_3$ and the mobility decreases as the concentration of Fe increases. From the results described in this work, similar to the effect on grain growth, Mg is more powerful in inhibiting GB

mobility than that of Fe. Bennison and Harmer also reported that Mg reduced GB mobility and proposed that the most plausible mechanism is solid-solution impurity drag [48, 53].

In reviewing the literature, no results were found on the influence of Fe on the GB mobility of $Al_2O_3$ while considering the separation between densification and grain growth during the sintering process. The present study experimentally measured the effective GB mobility of Fe-doped $Al_2O_3$. The data on the mobility of undoped $Al_2O_3$ had been reported in the literature. Through the same methods, the data $2.8 \times 10^{-15}$ $m^2/s$ of undoped polycrystalline $Al_2O_3$ in the present work is very close to the data $2.7 \times 10^{-15}$ $m^2/s$ reported by Akiva et al. [20] and is also in good agreement with the existing literature [96-101], as presented in Figure 28.

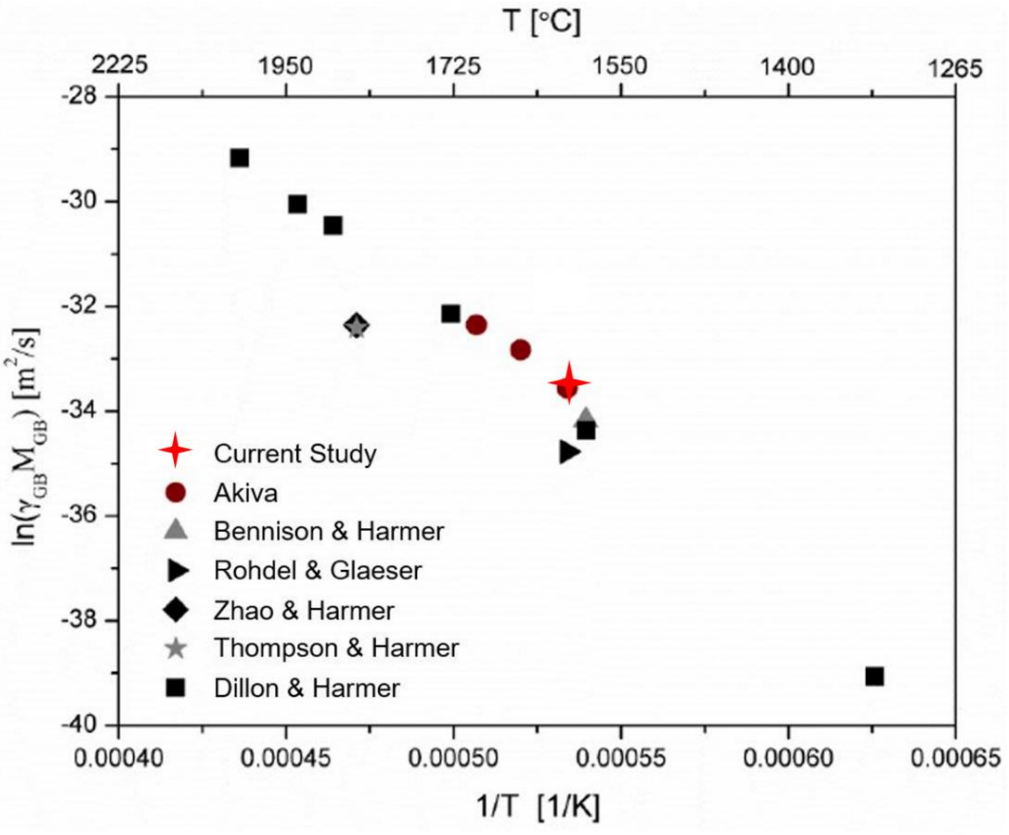


Figure 28: Effective GB mobility of undoped $Al_2O_3$ annealed in air, compared to effective mobility values from the literature. Redrawn from the data in [20].

Solute drag was introduced as a mechanism by which dopants hinder grain growth when the dopant concentration is under the solubility limit. For Mg in $Al_2O_3$[48], Y in tetragonal zirconia [102], Mg in tetragonal zirconia [103], Sc in $CeO_2$, and Yb in $CeO_2$ [104, 105], the solute drag was proposed as the basic force to inhibit grain growth and GB mobility. Solute drag is also applicable to this work as the mechanism for dopants (most present as trivalent Fe) reducing the GB mobility.

The solute drag of interstitials near the GB was thought to primarily result from the effect of the charge mismatch and size mismatch between the dopant and host ions in the GB region. For dopants of identical charge, cations size mismatch dominates the effect. The defect chemistry has been applied to analyze the possible mechanisms for accelerated or decelerated GB mobility. In the case of Mg in $Al_2O_3$, an interstitial mechanism (self-compensation) is energetically favorable as the solution mechanism. Given that Mg exists in $Al_2O_3$ below its solubility limits, it was found that doping $Al_2O_3$ with MgO introduces Mg interstitial atoms not only within the bulk $Al_2O_3$ but also in the GB area [106, 107]. It is assumed that the interstitials (i.e. segregation solutes) in the GB region create a solute-drag force that reduces the mobility of the GBs [6, 20]. In the case of CaO in $Al_2O_3$, an oxygen vacancy formation mechanism is energetically favorable and required for charge compensation. The increased mobility with Ca segregation is believed to be due to an increase in oxygen vacancy concentration in the vicinity of the GBs, thus facilitating faster GB motion [20, 22].

As for Fe (III) in $Al_2O_3$, Drahus et al. postulated that Fe segregation to the $Al_2O_3$ GBs retard GB migration [66]. Fe (mostly present in a trivalent state) decreased GB mobility in the present study, and also the segregation of Fe to a GB was experimentally confirmed by measuring the Fe excess in the GB region. This demonstrates the formation of Fe substitutionals near the boundary area. For $Fe^{3+}$, the solute drag of substitutional cations arises from the size mismatch of $Fe^{3+}$ and $Al^{3+}$. The ionic radii of the host ion and some dopants from the literature are listed in Table 6. $Al^{3+}$ has a size difference with $Fe^{3+}$ falling in between that with $Mg^{2+}$ and $Cr^{3+}$.

Table 6: The effective ionic radii of host ion and some dopants from literature and the size difference with trivalent Al.

| Ion | Ionic Radii [Å] (CN=6) | Size difference with $Al^{3+}$[Å] | Refs. |
|---|---|---|---|
| **$Al^{3+}$** | 0.67 | / | [33, 108] |
| **$Mg^{2+}$** | 0.86 | 0.19 | [33, 108] |
| **$Fe^{3+}$** | 0.78 | 0.11 | [108] |
| **$Cr^{3+}$** | 0.75 | 0.08 | [108] |
| **$Fe^{2+}$** | 0.92 | 0.25 | [108] |

In the case of Fe(II) in $Al_2O_3$, which would also be expected to segregate to the GBs it was revealed that $Fe^{2+}$ promoted grain growth and the mechanism was proposed that $Fe^{2+}$ improved the diffusive mass transport by segregation to high-energy non-basal GBs [65, 66]. It was argued that the influence of the compensating defects predominates. Given $Fe^{2+}$ in an $Al_2O_3$ system, it may be compensated for the charge by Al interstitials or oxygen vacancies. If the Al interstitials predominate, the $Fe^{2+}$ would introduce a drag to the GB rather than enhance its movement as reported. Therefore, we assume that the doping of $Fe^{2+}$ results in the formation of oxygen vacancies so as to compensate for the charge imbalance as presented in Eq. (22). It is postulated that the increased mobility with $Fe^{2+}$ segregation is due to the increase in vacancy concentration in the vicinity of the GBs, thus facilitating faster GB motion, similar to Ca in $Al_2O_3$.

$$O_O^* + 2Fe_{Al}^* = 2Fe_{Al}' + V_o^{\cdot\cdot} + \frac{1}{2}O_2(g) \qquad \text{Eq. (22)}$$

In summary, $Fe^{3+}$ solutes segregate to GBs in alumina to reduce the GB mobility, similar to Mg in $Al_2O_3$. Some $Fe^{2+}$ results in oxygen vacancies so as to compensate for the charge imbalance at GBs resulting in solute acceleration, similar to Ca in $Al_2O_3$. An anisotropic adsorption of $Fe^{3+}$ and/or $Fe^{2+}$ then results in an anisotropic grain growth.

# 6. Summary and Conclusions

The fundamental objectives of this research were to quantitatively study the influence of Fe (at contents below the solubility limit) on grain growth and GB mobility of $Al_2O_3$ sintered in air, to understand the effectiveness of Fe solutes on tailoring GB velocity compared to Mg, and to study the influence of Fe valence states on $Al_2O_3$ microstructure evolution. Furthermore, understanding the possible mechanism by which Fe affects GB mobility was also an important goal of this study.

The mobility of $Al_2O_3$ GBs was measured in samples that were doped with an increasing amount of Fe. With the increasing concentration of Fe dopant from 0.18 wt.% to 0.71 wt.% and 1.26 wt.%, the GB mobility of $Al_2O_3$ decreased from 2.6 $\times 10^{-15}$ $m^2/s$ to 1.3 $\times 10^{-15}$ $m^2/s$ and 4.1 $\times 10^{-16}$ $m^2/s$, respectively. Compared to the GB mobility of undoped $Al_2O_3$ (2.8 $\times 10^{-15}$ $m^2/s$), it can be seen that doping $Al_2O_3$ with Fe at concentrations below the solubility limit retards GB migration during annealing at 1600°C in air. The GB mobility decreased with increasing Fe concentration.

In addition, Mg is well known to inhibit GB mobility, and the combined influence of Fe and Mg in $Al_2O_3$ was studied. Mg at a concentration of ~0.01 wt.% reduced the $Al_2O_3$ GB mobility from 2.8 $\times 10^{-15}$ $m^2/s$ to 3.2 $\times 10^{-16}$ $m^2/s$. It can be summarized that both Mg and Fe decreased the GB mobility, but Mg exhibited a stronger drag effect on GBs in $Al_2O_3$ than that of Fe.

The mechanism by which Fe reduced GB mobility was postulated. The Fe excess at a GB was measured to be 3.6±1.4 Fe atoms/$nm^2$, at a detection limit of 1.8±0.6 Fe atoms/$nm^2$. $Fe^{3+}$ segregation to the GB region and thus introducing a solute drag could be the explanation for the decrease in GB mobility.

We also observed anisotropic grain structure in 2.93 wt.% Fe-doped $Al_2O_3$ after sintering at 1600 °C in air. The co-existence of the $Fe^{2+}$ and $Fe^{3+}$ in this sample was determined using XPS. $Fe^{3+}$ ions hindered GB motion (as concluded above) and $Fe^{2+}$

ions were reported to enhance grain growth in $Al_2O_3$. We derived a hypothesis that the presence of divalent Fe resulted in an increase of the oxygen vacancy concentration near the GBs to compensate for the charge imbalance, and this may accelerate the GB motion. A selective adsorption of $Fe^{3+}$ and/or $Fe^{2+}$ on different GBs then resulted in anisotropic grain growth.

# 7. Future Work

Future work on the influence of $Fe^{2+}$ on $Al_2O_3$ GB mobility should be completed. In particular, the precise ratio of different Fe valence states should be identified in the future.

Physical and chemical inhomogeneities are the common reason for local variation in the microstructure, which has often been considered as a major cause of abnormal grain growth. The local microstructural variations produce inequalities in the boundary mobility or energy, leading to abnormal growth [6]. To understand the inhomogeneous distribution of dopants at the microscale and its impact on the GB migration, we will try to build the correlation between the segregation of different Fe valence states with the characteristics of GBs, by using EBSD and electron energy loss spectroscopy (EELS).

Changing the oxygen partial pressure ($pO_2$) during sintering could be utilized to control the transition from $Fe^{3+}$ to $Fe^{2+}$. Therefore, additional research is needed to establish the influence of various $pO_2$ in the annealing atmosphere on Fe valence states, so as to investigate the influence of Fe on $Al_2O_3$ GB mobility in the valency version.

# 8. References


1. Barsoum, M., *Fundamentals of ceramics*. 2019: CRC press.
2. Kingery, W.D., H.K. Bowen, and D.R. Uhlmann, *Introduction to ceramics*. Vol. 17. 1976: John wiley & sons.
3. Burke, J. and D. Turnbull, *Recrystallization and grain growth.* Progress in metal physics, 1952. **3**: p. 220-292.
4. Rahaman, M.N., *Ceramic processing and sintering*. Vol. 1. 2017: CRC press.
5. Krill III, C.E., et al., *Extreme Abnormal Grain Growth: Connecting Mechanisms to Microstructural Outcomes.* Annual Review of Materials Research, 2023. **53**.
6. Powers, J. and A. Glaeser, *Grain boundary migration in ceramics.* Interface Science, 1998. **6**: p. 23-39.
7. Rohrer, G.S., et al., *Grain Boundary Migration in Polycrystals.* Annual Review of Materials Research, 2023. **53**.
8. Moshe, R., *The Influence of Dopants & Particles on the Kinetics of Microstructural Evolution of Alumina*, in *Materials Science and Engineering*. 2019, Technion-Israel Institute of Technology: https://kaplaninterfaces.net.technion.ac.il/theses/.
9. Gottstein, G. and L. Shvindlerman, *On the true dependence of grain boundary migration rate on driving force.* Scripta Metallurgica et Materialia, 1992. **27**(11): p. 1521-1526.
10. Gleiter, H., *The mechanism of grain boundary migration.* Acta Metallurgica, 1969. **17**(5): p. 565-573.
11. Gleiter, H., *Theory of grain boundary migration rate.* Acta Metallurgica, 1969. **17**(7): p. 853-862.
12. Sternlicht, H., et al., *The mechanism of grain growth at general grain boundaries in $SrTiO_3$.* Scripta Materialia, 2020. **188**: p. 206-211.
13. Newman, A.J., et al., *Modeling and model reduction for control and optimization of epitaxial growth in a commercial rapid thermal chemical vapor deposition reactor.* Institute for Systems Research, TR, 1998: p. 98-45.
14. Hirth, J. and R. Pond, *Steps, dislocations and disconnections as interface defects relating to structure and phase transformations.* Acta Materialia, 1996. **44**(12): p. 4749-4763.

15. Hirth, J., *Dislocations, steps and disconnections at interfaces.* Journal of Physics and Chemistry of Solids, 1994. **55**(10): p. 985-989.

16. Cai, W. and W.D. Nix, *Imperfections in crystalline solids*. 2016: Cambridge University Press.

17. Sternlicht, H., et al., *Characterization of grain boundary disconnections in SrTiO3 part I: the dislocation component of grain boundary disconnections.* Journal of Materials Science, 2019. **54**(5): p. 3694-3709.

18. Sun, X., et al., *Dislocation-induced stop-and-go kinetics of interfacial transformations.* Nature, 2022. **607**(7920): p. 708-713.

19. Wang, L., et al., *Tracking the sliding of grain boundaries at the atomic scale.* Science, 2022. **375**(6586): p. 1261-1265.

20. Akiva, R., A. Katsman, and W.D. Kaplan, *Anisotropic grain boundary mobility in undoped and doped alumina.* Journal of the American Ceramic Society, 2014. **97**(5): p. 1610-1618.

21. Moshe, R. and W.D. Kaplan, *The combined influence of Mg and Ca on microstructural evolution of alumina.* Journal of the American Ceramic Society, 2019. **102**(8): p. 4882-4887.

22. Moshe, R. and W.D. Kaplan, *The influence of CaO on alumina grain boundary mobility.* Journal of the European Ceramic Society, 2019. **39**(4): p. 1324-1328.

23. Chen, P.L. and I.W. Chen, *Grain boundary mobility in $Y_2O_3$: defect mechanism and dopant effects.* Journal of the American Ceramic Society, 1996. **79**(7): p. 1801-1809.

24. Kang, S.-J.L., *Sintering: densification, grain growth and microstructure*. 2004: Elsevier.

25. McHale, A.E., *Phase diagrams and ceramic processes*. 2012: Springer Science & Business Media.

26. Hundert, O., E. Nes, and N. Ryum, *On the zener drag—Addendum.* Acta Metallurgica, 1989. **37**(1): p. 129-133.

27. Humphreys, F.J. and M. Hatherly, *Recrystallization and related annealing phenomena*. 2012: Elsevier.

28. Lücke, K. and K. Detert, *A quantitative theory of grain-boundary motion and recrystallization in metals in the presence of impurities.* Acta Metallurgica, 1957. **5**(11): p. 628-637.

29. Cahn, J.W., *The impurity-drag effect in grain boundary motion.* Acta Metallurgica, 1962. **10**(9): p. 789-798.

30. Lücke, K. and H. Stüwe, *On the theory of impurity controlled grain boundary motion.* Acta Metallurgica, 1971. **19**(10): p. 1087-1099.

31. Dillon, S.J. and M.P. Harmer, *Multiple grain boundary transitions in ceramics: a case study of alumina.* Acta Materialia, 2007. **55**(15): p. 5247-5254.

32. Zamir, S., *Si segregation and its role in reaching transparent YAG.* Journal of the American Ceramic Society, 2017. **100**(4): p. 1689-1696.

33. Zamir, S., *The influence of cation additives on grain-boundary mobility in yttrium aluminum garnet (YAG).* Journal of the American Ceramic Society, 2015. **98**(1): p. 324-330.

34. Levin, I. and D. Brandon, *Metastable alumina polymorphs: crystal structures and transition sequences.* Journal of the American Ceramic Society, 1998. **81**(8): p. 1995-2012.

35. Swanson, H.E., *Standard X-ray diffraction powder patterns*. Vol. 25. 1953: US Department of Commerce, National Bureau of Standards.

36. Brandon, D. and W.D. Kaplan, *Microstructural characterization of materials*. 2013: John Wiley & Sons.

37. Bizot, P. and L. Sedel, *Alumina bearings in hip replacement: Theoretical and practical aspects.* Operative Techniques in Orthopaedics, 2001. **11**(4): p. 263-269.

38. Müller, J. and D. Neuschütz, *Efficiency of α-alumina as diffusion barrier between bond coat and bulk material of gas turbine blades.* Vacuum, 2003. **71**(1-2): p. 247-251.

39. Gluzer, G. and W.D. Kaplan, *Particle occlusion and mechanical properties of Ni–$Al_2O_3$ nanocomposites.* Journal of the European Ceramic Society, 2013. **33**(15-16): p. 3101-3113.

40. Yoshizawa, Y. and T. Sakuma, *Improvement of tensile ductility in high-purity alumina due to magnesia addition.* Acta Metallurgica et Materialia, 1992. **40**(11): p. 2943-2950.

41. Akiva, R., A. Berner, and W.D. Kaplan, *The solubility limit of CaO in $\alpha$-alumina at 1600°C.* Journal of the American Ceramic Society, 2013. **96**(10): p. 3258-3264.

42. Ghosh, P., et al., *The influence of temperature on the solubility limit of Ca in alumina.* Journal of the European Ceramic Society, 2020. **40**(15): p. 5767-5772.

43. Miller, L., A. Avishai, and W.D. Kaplan, *Solubility limit of MgO in $Al_2O_3$ at 1600° C.* Journal of the American Ceramic Society, 2006. **89**(1): p. 350-353.

44. Moshe, R., A. Berner, and W.D. Kaplan, *The solubility limit of $SiO_2$ in α-alumina at 1600° C.* Scripta Materialia, 2014. **86**: p. 40-43.

45. Wang, Y., et al., *High-temperature performance in $Al_2O_3$–$Cr_2O_3$ refractories: Effect of $Al_2TiO_5$.* Ceramics International, 2022. **48**(3): p. 3912-3922.

46. Bondioli, F., et al., *Reaction mechanism in alumina/chromia ($Al_2O_3$–$Cr_2O_3$) solid solutions obtained by coprecipitation.* Journal of the American Ceramic Society, 2000. **83**(8): p. 2036-2040.

47. Raghavan, V., *Al-Fe-O (aluminum-iron-oxygen).* Journal of Phase Equilibria and Diffusion, 2010. **31**(4): p. 367-367.

48. Bennison, S.J. and M.P. Harmer, *Effect of MgO solute on the kinetics of grain growth in A12O3.* Journal of the American Ceramic Society, 1983. **66**(5): p. C-90-C-92.

49. Brook, R., *Effect of $TiO_2$ on the initial sintering of $Al_2O_3$.* Journal of the American Ceramic Society, 1972. **55**(2): p. 114-114.

50. Grimes, R.W., *Solution of MgO, CaO, and $TiO_2$ in α-$AI_2O_3$.* Journal of the American Ceramic Society, 1994. **77**(2): p. 378-384.

51. Berry, K.A. and M.P. Harmer, *Effect of MgO solute on microstructure development in $Al_2O_3$.* Journal of the American Ceramic Society, 1986. **69**(2): p. 143-149.

52. Johnson, W. and R. Coble, *A test of the second-phase and impurity-segregation models for MgO-enhanced densification of sintered alumina.* Journal of the American Ceramic Society, 1978. **61**(3-4): p. 110-114.

53. Bennison, S.J. and M.P. Harmer, *Effect of Magnesia Solute on Surface Diffusion in Sapphire and the Role-of Magnesia in the Sintering of Alumina.* Journal of the American Ceramic Society, 1990. **73**(4): p. 833-837.

54. Altay, A. and M.A. Gülgün, *Microstructural evolution of calcium-doped α-alumina.* Journal of the American Ceramic Society, 2003. **86**(4): p. 623-29.

55. Bae, S.I. and S. Baik, *Determination of critical concentrations of silica and/or calcia for abnormal grain growth in alumina.* Journal of the American Ceramic Society, 1993. **76**(4): p. 1065-1067.

56. Horn, D.S. and G.L. Messing, *Anisotropic grain growth in $TiO_2$-doped alumina.* Materials Science and Engineering: A, 1995. **195**: p. 169-178.

57. Bagley, R.D., I.B. Cutler, and D.L. Johnson, *Effect of $TiO_2$ on initial sintering of $Al_2O_3$.* Journal of the American Ceramic Society, 1970. **53**(3): p. 136-141.

58. Powers, J.D., *Titanium effects on microstructure development in alumina*. 1997: University of California, Berkeley.

59. Powers, J. and A. Glaeser. *Titanium effects on sintering and grain boundary mobility of alumina*. in *Proceedings of the 21st Annual Conference on Composites, Advanced Ceramics, Materials, and Structures—B: Ceramic Engineering and Science Proceedings*. 1997. Wiley Online Library.

60. Kitayama, M. and A.M. Glaeser, *The Wulff Shape of Alumina: IV. Ti4+ -Doped Alumina.* Journal of the American Ceramic Society, 2005. **88**(12): p. 3492-3500.

61. Bae, I.J. and S. Baik, *Abnormal grain growth of alumina.* Journal of the American Ceramic Society, 1997. **80**(5): p. 1149-1156.

62. Dillon, S.J. and M.P. Harmer, *Relating grain boundary complexion to grain boundary kinetics II: silica -doped alumina.* Journal of the American Ceramic Society, 2008. **91**(7): p. 2314-2320.

63. Rao, W.R. and I.B. Cutler, *Effect of iron oxide on the sintering kinetics of $Al_2O_3$.* Journal of the American Ceramic Society, 1973. **56**(11): p. 588-593.

64. ZHAO, J. and M.P. HARMER, *Sintering of ultra -high -purity alumina doped simultaneously with MgO and FeO.* Journal of the American Ceramic Society, 1987. **70**(12): p. 860-866.

65. Tartaj, J. and G. Messing, *Anisotropic grain growth in α-$Fe_2O_3$-doped alumina.* Journal of the European Ceramic Society, 1997. **17**(5): p. 719-725.

66. Drahus, M., et al., *Densification and Grain Growth of Fe -Doped and Fe/Y Codoped Alumina: Effect of Fe Valency.* Journal of the American Ceramic Society, 2005. **88**(12): p. 3369-3373.

67. Lessing, P.A. and R.S. Gordon, *Creep of polycrystalline alumina, pure and doped with transition metal impurities.* Journal of Materials Science, 1977. **12**: p. 2291-2302.

68. Çelik, Y., et al., *Texture development in Fe-doped alumina ceramics via templated grain growth and their application to carbon nanotube growth.* Journal of the European Ceramic Society, 2013. **33**(6): p. 1093-1100.

69. Heiba, Z.K., et al., *Structural, optical, and electronic characterization of Fe-doped alumina nanoparticles.* Journal of Electronic Materials, 2018. **47**: p. 711-720.

70. Bataille, A., et al., *Deformation behaviour of iron-doped alumina.* Journal of the European Ceramic Society, 2005. **25**(6): p. 857-862.

71. Rhee, Y.-W., H.Y. Lee, and S.-J.L. Kang, *Diffusion induced grain-boundary migration and mechanical property improvement in Fe-doped alumina.* Journal of the European Ceramic Society, 2003. **23**(10): p. 1667-1674.

72. Gulicovski, J.J., L.S. Čerović, and S.K. Milonjić, *Point of zero charge and isoelectric point of alumina.* Materials and Manufacturing Processes, 2008. **23**(6): p. 615-619.

73. Reed, J., *Introduction to the principles of ceramic processing, Printed in the USA*. 1988, ISBN 0–471-59721-X, 156 p.

74. Lieberthal, M. and W.D. Kaplan, *Processing and properties of $Al_2O_3$ nanocomposites reinforced with sub-micron Ni and $NiAl_2O_4$.* Materials Science and Engineering: A, 2001. **302**(1): p. 83-91.

75. Standard, A., *Standard test methods for apparent porosity, water absorption, apparent specific gravity, and bulk density of burned refractory brick and shapes by boiling water.* West Conshohocken, PA.: ASTM C20-00, 2015.

76. Cliff, G. and G. Lorimer. *Quantitative analysis of thin metal foils using EMMA-4, the ratio technique*. in *Proceedings of the 5th European Congress on Electron Microscopy*. 1972. Institute of Physics.

77. Cliff, G. and G.W. Lorimer, *The quantitative analysis of thin specimens.* Journal of Microscopy, 1975. **103**(2): p. 203-207.

78. Merlet, C., *An accurate computer correction program for quantitative electron probe microanalysis.* Microchimica Acta, 1994. **114**: p. 363-376.

79. Berner, A., F. Gimelfarb, and T. Ukhorskaya, *Metrological aspects of micro-probe analysis.* Journal OF Analytical Chemistry of the USSR, 1982. **37**(2): p. 268-276.

80. Goldstein, J.I., et al., *Scanning electron microscopy and X-ray microanalysis*. 2017: Springer.

81. Mendelson, M.I., *Average grain size in polycrystalline ceramics.* Journal of the American Ceramic Society, 1969. **52**(8): p. 443-446.

82. Greczynski, G. and L. Hultman, *X-ray photoelectron spectroscopy: towards reliable binding energy referencing.* Progress in Materials Science, 2020. **107**: p. 100591.

83. Chastain, J. and R.C. King Jr, *Handbook of X-ray photoelectron spectroscopy.* Perkin-Elmer Corporation, 1992. **40**: p. 221.

84. Seah, M. and D. Briggs, *Instrument calibration for AES and XPS.* Surface analysis by Auger and X-ray photoelectron spectroscopy, 2003: p. 167-189.

85. Keast, V. and D. Williams, *Quantification of boundary segregation in the analytical electron microscope.* Journal of Microscopy, 2000. **199**(1): p. 45-55.

86. Yamashita, T. and P. Hayes, *Analysis of XPS spectra of $Fe^{2+}$ and $Fe^{3+}$ ions in oxide materials.* Applied surface science, 2008. **254**(8): p. 2441-2449.

87. Sherwood, P.M., *Curve fitting in surface analysis and the effect of background inclusion in the fitting process.* Journal of Vacuum Science & Technology A: Vacuum, Surfaces, and Films, 1996. **14**(3): p. 1424-1432.

88. Salvi, A.M., et al., *Peak fitting of the chromium 2p XPS spectrum.* Applied Surface Science, 1995. **90**(3): p. 333-341.

89. Biesinger, M.C., et al., *Resolving surface chemical states in XPS analysis of first row transition metals, oxides and hydroxides: Cr, Mn, Fe, Co and Ni.* Applied Surface Science, 2011. **257**(7): p. 2717-2730.

90. Pratt, A., I. Muir, and H. Nesbitt, *X-ray photoelectron and Auger electron spectroscopic studies of pyrrhotite and mechanism of air oxidation.* Geochimica et Cosmochimica Acta, 1994. **58**(2): p. 827-841.

91. Kaplan, W.D., et al., *Ca Segregation to Basal Surfaces in α-Alumina.* Journal of the American Ceramic Society, 1995. **78**(10): p. 2841-2844.

92. Shaheen, W., *Thermal behaviour of pure and binary Fe $(NO_3)_3 \cdot 9H_2O$ and $(NH_4)\ 6Mo_7O_{24} \cdot 4H_2O$ systems.* Materials Science and Engineering: A, 2007. **445**: p. 113-121.

93. Gadalla, A.M. and H.-F. Yu, *Thermal decomposition of Fe (III) nitrate and its aerosol.* Journal of Materials Research, 1990. **5**(6): p. 1233-1236.

94. Manor, E., *Grain growth inhibition in nanocrystalline alumina doped with chromia.* Nanostructured Materials, 1997. **8**(3): p. 359-366.

95. Park, C.W. and D.Y. Yoon, *Effects of $SiO_2$, $CaO_2$, and MgO additions on the grain growth of alumina.* Journal of the American Ceramic Society, 2000. **83**(10): p. 2605-2609.

96. Bennison, S.J. and M.P. Harmer, *Grain-growth kinetics for alumina in the absence of a liquid phase.* Journal of the American Ceramic Society, 1985. **68**(1): p. C-22-C-24.

97. Zhao, J. and M.P. Harmer, *Effect of pore distribution on microstructure development: III, model experiments.* Journal of the American Ceramic Society, 1992. **75**(4): p. 830-843.

98. Thompson, A.M. and M.P. Harmer, *Influence of Atmosphere on the Final-Stage Sintering Kinetics of Ultra-High-Purity Alumina.* Journal of the American Ceramic Society, 1993. **76**(9): p. 2248-2256.

99. Dillon, S.J. and M.P. Harmer, *Intrinsic grain boundary mobility in alumina.* Journal of the American Ceramic Society, 2006. **89**(12): p. 3885-3887.

100. Bae, S.I. and S. Baik, *Sintering and grain growth of ultrapure alumina.* Journal of Materials Science, 1993. **28**: p. 4197-4204.

101. Rödel, J. and A.M. Glaeser, *Anisotropy of grain growth in alumina.* Journal of the American Ceramic Society, 1990. **73**(11): p. 3292-3301.

102. Lee, I. and C. I-W, *Sintering and grain growth in tetragonal and cubic zirconia.* Sintering'87., 1987. **1**: p. 340-345.

103. Hwang, S.L. and I.W. Chen, *Grain size control of tetragonal zirconia polycrystals using the space charge concept.* Journal of the American Ceramic Society, 1990. **73**(11): p. 3269-3277.

104. Chen, P.L. and I.W. Chen, *Role of defect interaction in boundary mobility and cation diffusivity of $CeO_2$.* Journal of the American Ceramic Society, 1994. **77**(9): p. 2289-2297.

105. Chen, P.-L. and I.-W. Chen, *Grain growth in $CeO_2$: dopant effects, defect mechanism, and solute drag.* 1996.

106. Marcus, H. and M. Fine, *Grain-Boundary Segregation in MgO-Doped $Al_2O_3$.* Journal of the American Ceramic Society, 1972. **55**(11): p. 568-570.

107. Yan, M., R. Cannon, and H. Bowen, *Space charge, elastic field, and dipole contributions to equilibrium solute segregation at interfaces.* Journal of Applied Physics, 1983. **54**(2): p. 764-778.

108. Shannon, R.D., *Revised effective ionic radii and systematic studies of interatomic distances in halides and chalcogenides.* Acta crystallographica section A: crystal physics, diffraction, theoretical and general crystallography, 1976. **32**(5): p. 751-767.

# השפעת ברזל על ניידות של גבולות גרעינים באלומינה

חיבור על מחקר

לשם מילוי חלקי של הדרישות לקבלת התואר
מגיסטר למדעים בהנדסת חומרים

**שיניאן וו**

הוגש לסנט הטכניון – מכון טכנולוגי לישראל

ניסן ה'תשפ"ד חיפה אפריל 2024